Department of Physics and Astronomy
University of Heidelberg

Bachelor Thesis in Physics
submitted by

Florian Reiß

born in Heidelberg (Germany)

2014

Sensitivity Study of the Phase I Detector for the Mu3e Experiment

This Bachelor Thesis has been carried out by Florian Reiß at the
Physikalisches Institut in Heidelberg
under the supervision of
Dr. Niklaus Berger

Abstract

The Mu3e Experiment searches for the lepton-flavour violating decay $\mu^+ \to e^+e^+e^-$. This decay is heavily suppressed in the Standard Model, so its observation would indicate the presence of new physics. To reach the planned sensitivity of better than one in 10^{16} decays, the experiment uses an innovative thin silicon pixel detector. In later phases, timing detectors based on scintillating fibres and tiles will be added.

There is an extensive simulation of the experiment based on GEANT4, as well as software for track and vertex reconstruction. The properties of this software were examined for simulations of the first detector phase. The invariant masses of $\mu^+ \to e^+e^+e^-$ and background caused by radiative muon decays with internal conversion were reconstructed for various simulation scenarios and the sensitivity for the first phase of detector operation was estimated.

Zusammenfassung

Das Mu3e-Experiment sucht nach dem Leptonenzahl-verletzendem Zerfall $\mu^+ \to e^+e^+e^-$. Da dieser Zerfall im Standardmodell stark unterdrückt ist, würde die Beobachtung auf neue Physik hindeuten. Um die geplante Sensitivität von besser als einen in 10^{16} Zerfällen zu erreichen, benutzt das Experiment innovative Silikon-Pixeldetektoren. In späteren Phasen werden Zeitdetektoren basierend auf szintillierenden Fasern und Kacheln hinzugefügt.

Es existiert eine umfangreiche Simulation des Experiments basierend auf GEANT4, sowie Software zur Spur- und Vertexrekonstruktion. Die Eigenschaften dieser Software wurden für Simualtionen der ersten Detektorphase untersucht. Weiterhin wurden die invarianten Massen von $\mu^+ \to e^+e^+e^-$ und Untergrund durch radiative Muon-zerfälle mit interner Konversion für verschiedene Simulationsszenarien rekonstruiert und die Sensitivität für die erste Detektorphase ermittelt.

Contents

List of Figures

List of Tables

Chapter I

Introduction

1 The Standard Model Of Particle Physics

The Standard Model (SM) describes the particles which make up matter and their interactions. It divides these particles into three generations of quarks and leptons respectively, as seen in Fig. 1. Their interactions (strong, weak and electromagnetic) are mediated by gauge bosons. For every particle x there is a corresponding anti-particle $\bar{x}$.
The quarks are up, down, charm, strange, top and bottom. Up and down quarks are the constituents of protons and neutrons making up atomic nuclei. The leptons are electron, muon and tau which are charged and the corresponding neutral (electron-, muon, tau-) neutrinos.
The gauge bosons are the photon mediating the electromagnetic force, the W^+-, W^-- and Z- bosons mediating the weak interaction and the gluons mediating the strong interaction.

The SM is confirmed by a multitude of experiments and is a great success of modern physics. One of the latest achievements is the observation of the Higgs boson which is thought to give mass to particles and thus completing the SM. However, there are still questions left open by the SM such as the nature of dark matter, the inclusion of gravitation and the matter-antimatter asymmetry in the universe.

One approach to get closer to solutions to these problems is to look at lepton flavour violation. Each lepton generation has a corresponding lepton flavour number $L_{e,\mu,\tau}$. A lepton is assigned a lepton

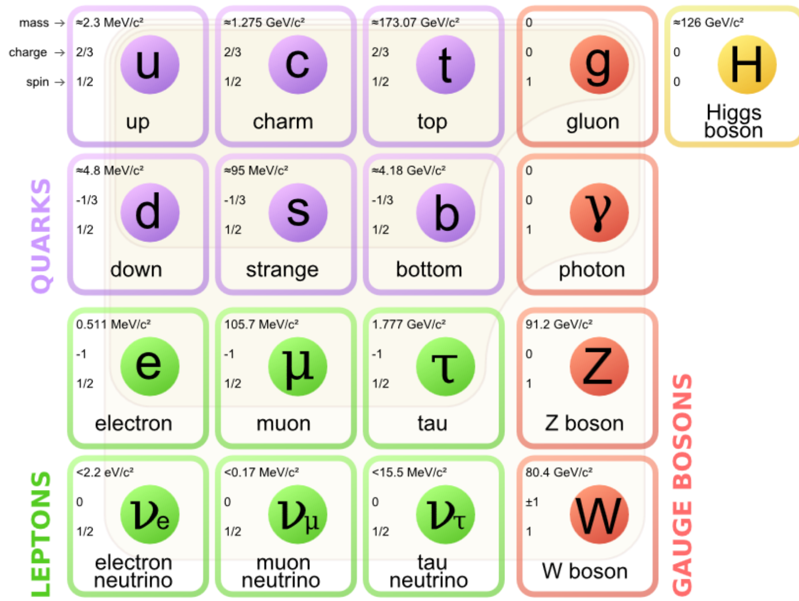

Figure 1: Standard Model of particle physics[1]

flavour number of +1 whereas an anti-lepton is assigned a number of -1. The total lepton flavour number was considered to be a conserved quantity in physical processes like decays, but experiments have already shown that there are neutrino-oscillations violating this. Also the masses of the neutrinos have been found to been non-zero as opposed to zero in the SM. To account for these, extensions to the SM were necessary allowing for neutrino oscillations.

2 The Mu3e Experiment

The Mu3e experiment is looking for the lepton flavour violating decay of one muon μ^+ into two positrons e^+ and one electron e^-: $\mu^+ \to e^+e^+e^-$. The SINDRUM experiment concluded in 1988 that the branching ratio is smaller than 10^{-12} at 90% confidence level [2]. That the electron and muon flavour number conservation are violated is easily seen: Before the decay we have $L_e = 0, L_\mu = -1$, after we have $L_e = -1, L_\mu = 0$.

This decay is highly suppressed to BR $< 10^{-54}$ [3] in the SM where it can be mediated by neutrino oscillations as shown in Fig. 2.

Detecting this decay at higher branching fractions would indicate the presence of new physics beyond the Standard Model. Such new physics could be models where $\mu \rightarrow 3e$ is possible via supersymmetric particles in a loop as shown in Fig. 3. A overview of other possible models is given in [3]. To detect this decay or to push down the limit on its branching fraction is the aim of the Mu3e experiment.

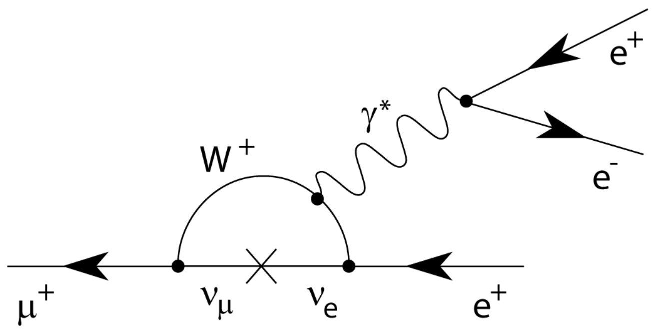

Figure 2: $\mu \rightarrow 3e$ via neutrino oscillation [3]

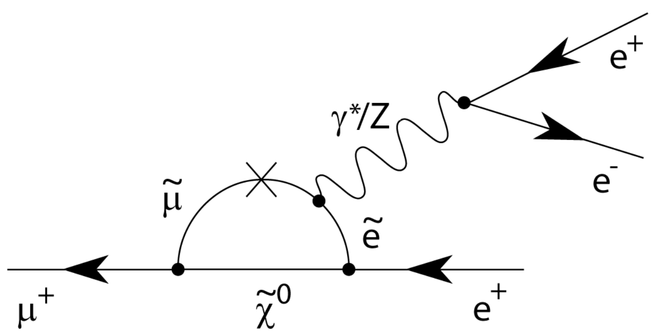

Figure 3: $\mu \rightarrow 3e$ via supersymmetry [3]

2.1 Muon Decay

In the Mu3e Experiment muons will be stopped on a target where they decay. Because the muons are almost at rest when the decay the resulting tracks of the three decay particles have specific qualities which will be used to identify a signal event. First, the resulting tracks originate from the same vertex.
Second, because of conservation of momentum, the sum of the mo-

Name	Mode	Branching Fraction
Michel decay	$\mu \to e^+ \nu_e \bar{\nu_\mu}$	$\approx 100\%$
Radiative decay	$\mu \to e^+ \nu_e \bar{\nu_\mu} \gamma$	$(1.4 \pm 0.4)\%$
Internal conversion	$\mu \to e^+ \nu_e \bar{\nu_\mu} e^+ e^-$	$(3.4 \pm 0.4) \cdot 10^{-5}$

Table 1: Lepton flavour conserving muon decays. In the radiative decay only events with a photon energy $E_\gamma > 10 MeV$ are included. Adapted from [4].

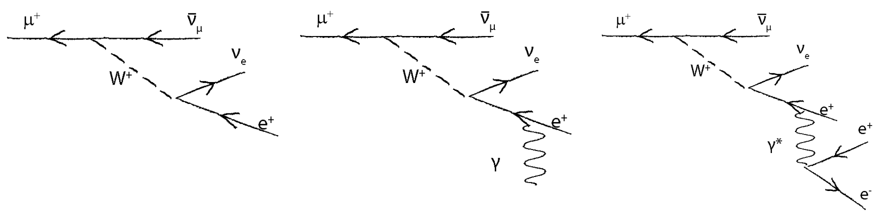

(a) Michel decay (b) Radiative decay (c) Radiative decay with internal conversion

Figure 4: Lepton flavour conserving muon decays.

menta $\vec{p_i}$ of the decay particles should be zero:

$$\sum_{i=1}^{3} \vec{p_i} = 0 \tag{1}$$

This also means that the momenta are in a plane. Because of conservation of energy the 4-vectors $\vec{P_i}$ must fulfil:

$$m_\mu^2 = |\sum_{i=1}^{3} \vec{P_i}|^2 \tag{2}$$

with the muon mass m_μ.

From these considerations follows that the maximal momentum of one decay particle can not be larger than half the muon mass.

2.2 Background

There are several types of background events which have to be accounted for to reach the desired sensitivity limit. The background is caused by the lepton flavour conserving decay channels of the muon with branching fractions much larger than $\mu \to eee$ (see Tab. 1 and Fig. 4).

Internal Conversion Background

The main background source is the radiative muon decay with internal conversion where one muon decays into two positrons and one electron with two additional neutrinos as seen in Fig. 5.

$$\mu^+ \rightarrow e^+ e^+ e^- \nu_e \bar{\nu_\mu} \tag{3}$$

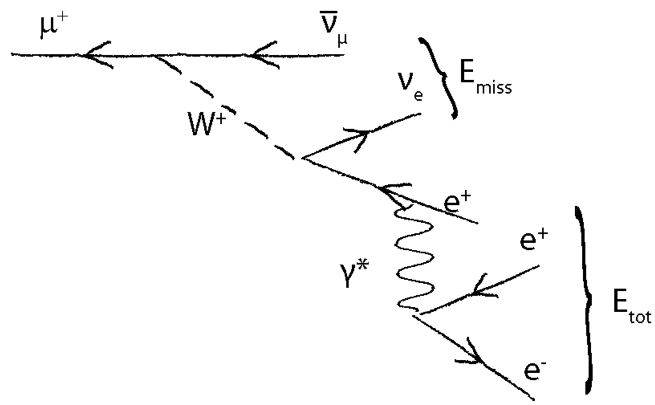

Figure 5: Radiative muon decay with internal conversion. E_{tot} denotes the measurable energy, E_{miss} the energy carried away by neutrinos.

The neutrinos can not be detected but carry away momentum and energy so this background can be distinguished from the signal by looking at sum of the momenta which is here non-zero and the total energy which is not equal to the muon mass. For this a good momentum resolution of the detector is required. Fig. 6 shows the branching ratio as function of the missing energy $E_{miss} = m_\mu - E_{tot}$. At the desired sensitivity of 10^{-16} the background is about 1.4 MeV distant from the signal at m_μ, so the resolution has be better than this. To be more precise, Fig. 7 shows the fraction of internal conversion events in the signal region against the resolution of the mass reconstruction for different σ-regions around the muon mass. From this follows that the average momentum resolution has to be better than 0.5 MeV to reach a sensitivity of 10^{-16}.

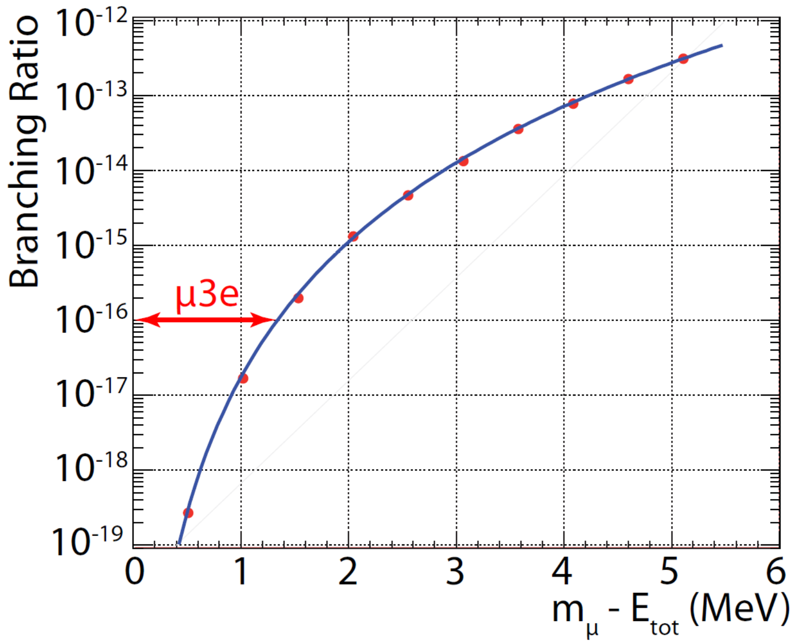

Figure 6: Branching fraction of internal conversion against missing energy [5].

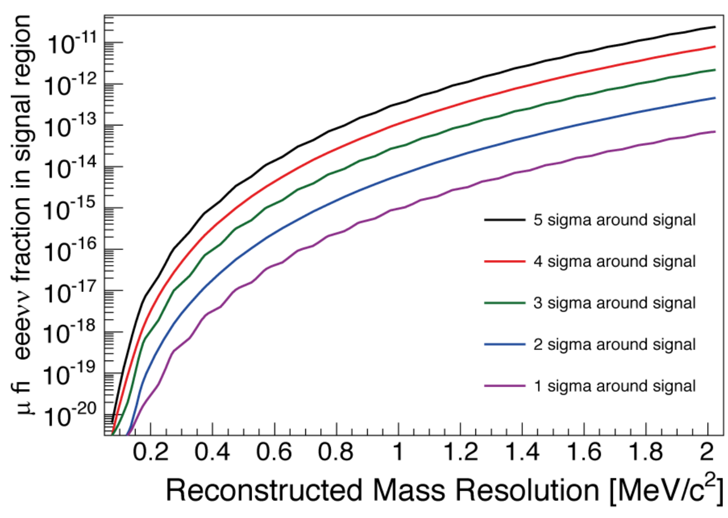

Figure 7: Fraction of internal conversion events in the signal region against the resolution of the mass reconstruction [3].

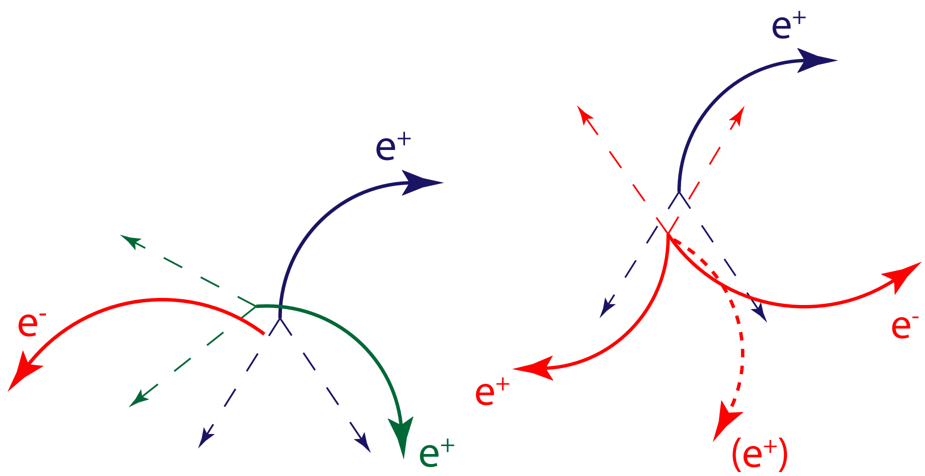

(a) Combination of two Michel decays with one electron

(b) Combination of one Michel decay with internal conversion

Figure 8: Examples for accidental background.

Accidental Background

Another kind of background is due to accidental combinations of electrons and positrons. These can originate from internal conversion, but also from ordinary Michel decays, radiative decays and scattering in the target and detector material. Examples for accidental combinations can be seen in Fig. 8. As shown, a possible combination could be two positrons from different Michel decays and one electron or one electron and positron from internal conversion with an additional positron from a Michel decay.

The tracks of accidental background usually do not share a common vertex, the total momentum and energy and the timing of the hits in the detector do not show the qualities of a signal event. All this can be used to suppress accidental background. Therefore a good vertex resolution, a good timing resolution and again a good momentum resolution is required.

2.3 Experimental Challenges

The aim of the Mu3e experiment is to push the current limit of $\mathcal{O}(10^{-12})$ set by the SINDRUM experiment [2] to $\mathcal{O}(10^{-16})$. To reach this sensitivity in a reasonable running time a high rate muon beam is required (up to $\approx 2 \cdot 10^9 \frac{muons}{s}$ in phase II [3]). To reduce the accidental background, good timing, vertex position and momentum resolutions are required. The separation of signal from internal conversion can only be done via good momentum resolution.

2.4 Multiple Scattering

Multiple Coulomb scattering is the determining factor for the momentum resolution in the Mu3e experiment. It is caused by the Coulomb interaction of charged particles with the nuclei of a material they traverse and results in a deflection from the original trajectory by an offset y_{plane} and angle θ_{plane} as seen in Fig. 9. The core of the distribution of θ can be described by a Gaussian distribution with a σ given by the Highland formula [4]:

$$\sigma_\theta = \frac{13.6\text{MeV}}{\beta c p} z \sqrt{\frac{x}{X_0}} \left[1 + 0.038 \ln(\frac{x}{X_0})\right], \tag{4}$$

with z the particle's charge, βc its velocity, p its momentum, x the material thickness and X_0 the radiation length of the material. As seen in the formula, the effect of Multiple scattering is larger for low momentum particles.

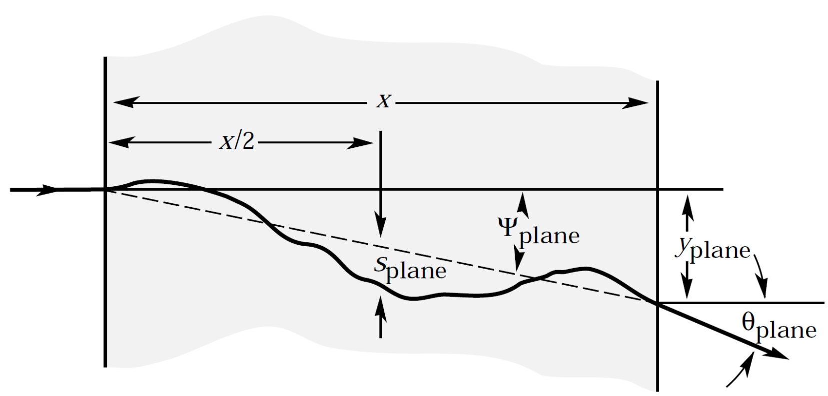

Figure 9: Multiple Coulomb scattering [4]

2.5 Detector

The detector for the Mu3e experiment will be built in several phases (Figs. 10 - 12), namely phases I and II where phase I is split up in

IA and IB. In phase IA the experiment is run with a minimal detector set-up consisting of the hollow double-cone target and inner and outer double layers of silicon pixel detectors. In phase IB scintillating fibres, recurl stations and tile detectors are added. In the final stage II another recurl station with tile detectors is added. The additional pixel layers in the recurl stations improve momentum resolution, due to the large lever arm for tracks recurling in the magnetic field, while the scintillating fibres and tiles improve time resolution. In each phase a solenoidal magnetic field of 1 T will bend the tracks of the decay particles allowing reconstruction of the track momenta.

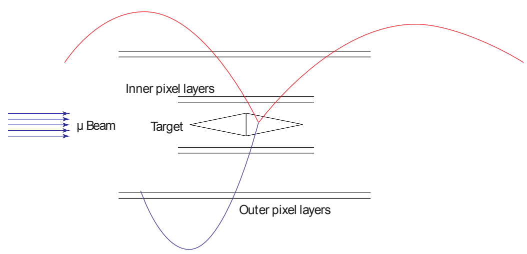

Figure 10: Phase IA detector. Minimal design with only target and two pixel layers [3].

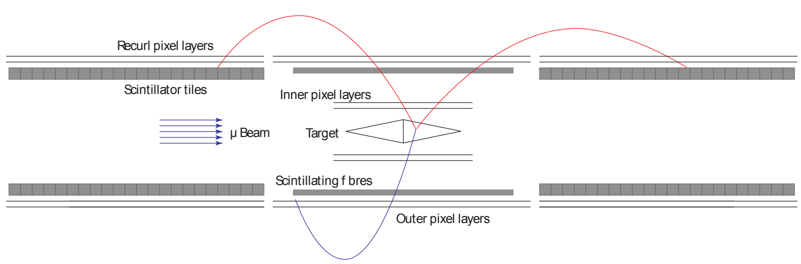

Figure 11: Phase IB detector. Scintillating fibres and recurl stations with additional pixel layers and tile detectors [3].

The experiment will be conducted at the Paul Scherrer Institut (PSI) in Switzerland.

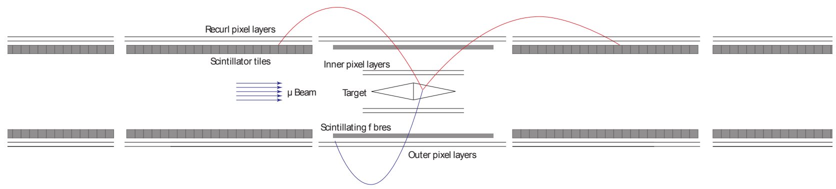

Figure 12: Phase II detector. Additional recurl stations are added. The stations on the left and right are shortened for this illustration [3].

2.6 Detector Components

Pixel detector

The dominating factor on momentum resolution is not the pixel size of the detector, but multiple Coulomb scattering in the detector material. Therefore the material budget should be minimized. The Mu3e experiment will use silicon High-Voltage Monolithic Active Pixel Sensors (HV-MAPS) [6] with a pixel size of $80 \cdot 80\ \mu\text{m}^2$ and a thickness of $50\ \mu$m keeping the influence of multiple scattering as low as possible. The read-out is done in frames of 50 ns.

Fibre detector

The fibre detectors placed between the two pixel layers allow for a time resolution ≤ 1 ns [7]. The material budget has to be kept in mind to reduce the effect of multiple scattering on momentum resolution.

Recurl station

The recurl stations feature pixel detectors similar to the central ones. The scintillating tile detectors provide a time resolution better than 100 ps [8, 9]. The particles are stopped in or after the tile detector, so it can be thicker compared to the fibre detector.

Chapter II

Simulation and Reconstruction

3 Simulation

A detailed simulation exists to study the expected properties of the Mu3e experiment. This is done in order to confirm that the desired results can be reached, to find possible improvements for the detector design and to try out other configurations. In addition, the software used for data analysis can be tested and prepared for the actual runs. The simulation allows a comparison between the true values from the Monte-Carlo generation with the measured ones for calibration and efficiency studies.

For this purpose a GEANT4 [10] simulation of the Mu3e experiment exists which is an extensive geometric simulation of the detector and the interactions of particles with matter based on Monte-Carlo methods. The decay of muons stopped on the target via Michel decays, internal conversions and signal events are simulated depending on the simulation settings. The tracks of the decay particles are propagated and the hits in the detector layers are registered.

Besides the number of frames to be simulated and a seed for the random number generator, various properties of the simulation of which some are described in the following can be changed. The full configuration files can be seen in Appendix A.

Readout frame length Length of one readout frame in ns.

Muon rate Rate of incoming muons in $\frac{1}{s}$.

Signal branching fraction Branching fraction for $\mu \to 3e$ events.

Special decay mode Determines decay mode. In addition to ordinary decays, there are settings allowing for special decay modes for various purposes. Certain decay mode guarantees one signal event or one radiative decay with or without internal conversion per frame to study these types of events. Other configurations overlay two or three signal, Michel, radiative or internal conversion events from the same vertex. This can be used to test the separation of signal and background and suppression of combinatorics without using vertex suppression.

Tracker threshold Minimal energy in MeV needed to be deposited by a traversing particle to be registered as a hit in the pixel detector.

Tracker efficiency Probability that a particle traversing a detector layer is also registered as a hit in the pixel detector. Allows the study of the influence of non perfect detectors on the efficiency of detecting a signal event.

Small/large sensor thickness thickness of the inner/outer detector layer in μm. Allows the study of the influence of detector material on the momentum resolution.

Number fibre layers number of layers of scintillating fibres in the detector(phase IB and II). Can be used to demonstrate the effect of additional material on the momentum resolution.

Small/large sensor pixel size pixel size of inner/outer detector layer.

Internal conversion mass cut cut on simulated internal conversion events. Can be set to high values to run simulation without internal conversion. Is also used to reduce run time by simulating only internal conversion events in interesting mass areas, usually close to the muon mass.

3.1 Physical Processes

The following section is adapted from [3].

Michel decay

Michel decays are implemented in GEANT4 considering the polarization of muons based on [11] and [12]. The neutrino spectra do not follow the physical distribution, but this is irrelevant for the simulation for Mu3e as the neutrinos are not detected. The matrix element for Michel decays contain radiative corrections and is not clearly separated from the radiative matrix element which could lead to inaccuracies.

Radiative decay

The TWIST collaboration [13] implemented radiative muon decays in GEANT4 based on [14]. The neutrino spectra are not included.

Radiative decay with internal conversion

To simulate radiative decays with internal conversion events are generated evenly in phase space with RAMBO (RAndom Momenta BOoster) [15] and then selected utilizing the hit and miss technique applying the matrix element from [5]. Simulating the complete phase space would result in high running times because of the computationally intensive hit and miss method. To reduce run time, only regions of interest can be simulated. For example the events can be restricted to high invariant masses (see 'Internal conversion mass cut' above). The muons in the beam are polarized (spins aligned in one direction), the used matrix element however is not, resulting in a non-polarized simulation. It is not entirely clear if this has a significant effect on the results.

The simulations of all three decays can be improved and is under ongoing research.

4 Track Reconstruction

The following section summarizes [16]. To reconstruct the helical tracks of the charged decay particles in the the solenoidal magnetic field a novel track fitting algorithm has been established to provide a fast online track reconstruction. It assumes a perfect measurement of hit positions and only considers uncertainties introduced by multiple scattering. The momentum and energy of a particle is assumed to be conserved. Also it is assumed that the material causing multiple scattering lies in the same plane as the sensitive plane where the hit positions are measured.

As seen in Fig. 13 the hits of a track are divided into overlapping triplets which are fitted separately and then combined to track segments. The detector geometry determines the number of hits and triplets a track segment can be made of: The minimum requirements to reconstruct a track segment are four hits —two in the inner and two in the outer layer— divided into two triplets. A recurling particle can produce another two to four hits making track segments with six hits divided into 4 triplets and 8 hits divided into 6 triplets.

To describe the track fit for one triplet several parameters are introduced as seen in Fig. 14. The z-axis of the coordinate system is defined by the direction of the magnetic field (longitudinal), while the x-y-plane is the plane transversal to the magnetic field. The variables θ or Θ describe polar angles and ϕ or Φ describe azimuthal angles.

We have a triplet with the hit positions $\vec{x_0}$, $\vec{x_1}$ and $\vec{x_2}$. The effects of multiple scattering are taken into account in the middle hit of the triplet creating a kink in the trajectory. Multiple scattering is described by the angles Φ_{MS} in the transverse plane and Θ_{MS} in the longitudinal plane.

The aim of the triplet fit is to find the three-dimensional radius R_{3D} which minimizes the multiple scattering angles. This done by minimizing following χ^2:

$$\chi^2(R_{3D}) = \frac{\Theta_{MS}(R_{3D})^2}{\sigma_\theta^2} + \frac{\Phi_{MS}(R_{3D})^2}{\sigma_\phi^2} \tag{5}$$

This is equivalent to:

$$0 = \frac{d\Theta_{MS}}{dR_{3D}} \frac{\Theta_{MS}}{\sigma_\theta^2} + \frac{d\Phi_{MS}}{dR_{3D}} \frac{\Phi_{MS}}{\sigma_\phi^2} \tag{6}$$

For most purposes the uncertainties σ_θ and σ_ϕ can be assumed to be the same ($\sigma_\theta = \sigma_\phi$), so the equation can be simplified:

$$0 = \frac{d\Theta_{MS}}{dR_{3D}} \Theta_{MS} + \frac{d\Phi_{MS}}{dR_{3D}} \Phi_{MS} \tag{7}$$

The three-dimensional radius can be related to the track momentum for a track in a magnetic field of magnitude B:

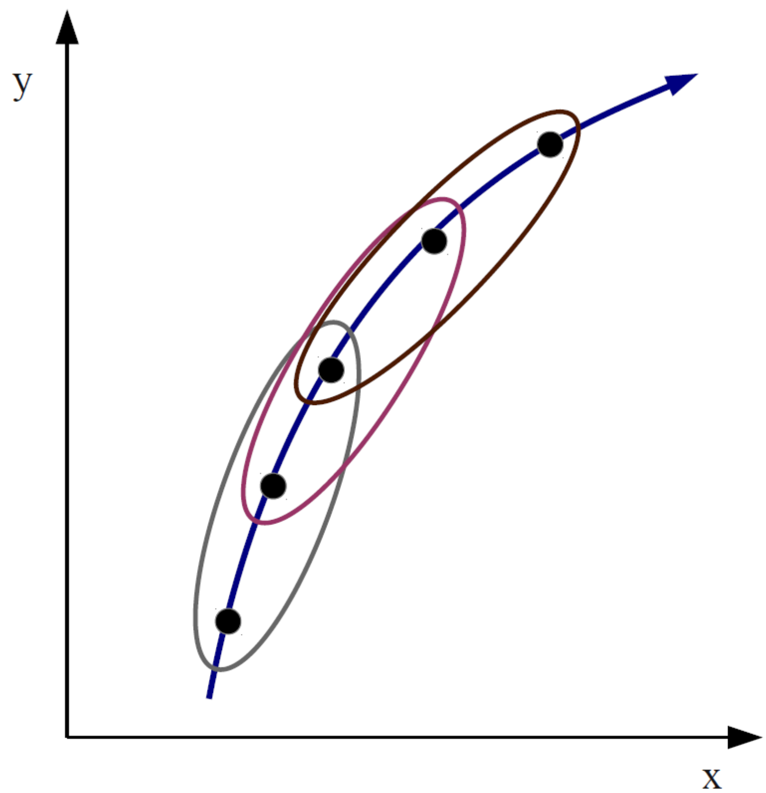

Figure 13: Hits of a track divided in overlapping triplets [16]

$$p \approx 0.3 \cdot R_{3D} B \frac{MeV}{mm\,T} \tag{8}$$

To find this radius the functions $\Theta_{MS}(R_{3D})$ and $\Phi_{MS}(R_{3D})$ are needed. In the transversal plane ϕ_{01} is the angle between the line connecting the first and second hit and the x-axis, ϕ_{12} the angle between the line connecting the second and third hit and the x-axis. R_1 and R_2 are the transverse radii before and after scattering. Φ_1 and Φ_2 are the bending angles. $\vec{d_{01}}$ and $\vec{d_{12}}$ are the vectors directly connecting the hits.

In the longitudinal plane z_{01} and z_{12} are the distances between the hits in z-direction and Θ_0 and Θ_1 the polar angles.

These variables are connected [16]:

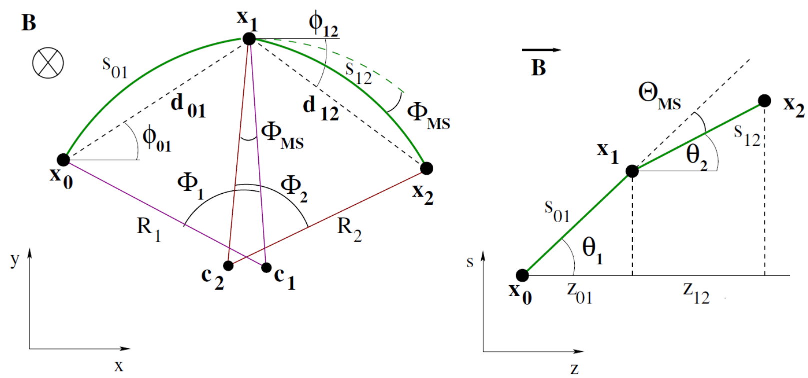

Figure 14: Geometric sketch for the triplet fit for the transverse (left) and longitudinal (right) plane [16]

$$2(\phi_{12} - \phi_{01}) = \Phi_1 + \Phi_2 + 2\Phi_{MS} \tag{9}$$

$$R_1 = \frac{d_{01}}{2\sin(\Phi_1/2)} \quad R_2 = \frac{d_{12}}{2\sin(\Phi_2/2)} \tag{10}$$

Insert (10) in (9):

$$\phi_{12} - \phi_{01} = \arcsin(\frac{d_{01}}{2R_1}) + \arcsin(\frac{d_{12}}{2R_2}) \tag{11}$$

The three-dimensional bending radius R_{3D}, which is conserved, if the total momentum is conserved (which is assumed here), is related to the transverse bending radii:

$$R_{3D}^2 = R_1^2 + \frac{z_{01}^2}{\Phi_1^2} = R_2^2 + \frac{z_{12}^2}{\Phi_2^2} \tag{12}$$

From this the equations for $\Theta_{MS}(R_{3D})$ and $\Phi_{MS}(R_{3D})$ can be obtained.

The three-dimensional radius minimizing the χ^2 defined in (32) is found by linearising around a solution without multiple scattering. This approach is justified because the multiple scattering angles are small.

Around the approximate solution $R_{3D,0}$ with the scattering angles $\Phi_{MS,0} = \Phi_{MS}(R_{3D,0})$ and $\Theta_{MS,0} = \Theta_{MS}(R_{3D,0})$ a Taylor expansion is done:

$$\Theta_{MS}(R_{3D,0}+\Delta R_{3D}) = \Theta_{MS,0} + \Delta R_{3D}\frac{\partial\Theta_{MS}}{\partial R_{3D}} + 0.5\Delta R_{3D}^2\frac{\partial^2\Theta_{MS}}{\partial R_{3D}^2} + ..$$
$$\Phi_{MS}(R_{3D,0}+\Delta R_{3D}) = \Phi_{MS,0} + \Delta R_{3D}\frac{\partial\Phi_{MS}}{\partial R_{3D}} + 0.5\Delta R_{3D}^2\frac{\partial^2\Phi_{MS}}{\partial R_{3D}^2} + .. \tag{13}$$

where ΔR_{3D} is a small correction: $R_{3D} = R_{3D,0} + \Delta R_{3D}$.

Then the ΔR_{3D}^{min} minimizing χ^2 can be found (neglecting second order and higher terms):

$$\Delta R_{3D}^{min} = -\frac{\frac{d\Theta_{MS}}{dR_{3D}}\Theta_{MS,0} + \frac{d\Phi_{MS}}{dR_{3D}}\Phi_{MS,0}}{\left(\frac{d\Theta_{MS}}{dR_{3D}}\right)^2 + \left(\frac{d\Phi_{MS}}{dR_{3D}}\right)^2} \tag{14}$$

$$\chi^2_{min} = \frac{1}{\sigma^2_{MS}}\left(\Theta^2_{MS,0} + \Phi^2_{Ms,0} - \frac{\left(\frac{d\Theta_{MS}}{dR_{3D}}\Theta_{MS,0} + \frac{d\Phi_{MS}}{dR_{3D}}\Phi_{MS,0}\right)^2}{\left(\frac{d\Theta_{MS}}{dR_{3D}}\right)^2 + \left(\frac{d\Phi_{MS}}{dR_{3D}}\right)^2}\right) \tag{15}$$

with the second derivative:

$$\left(\chi^2\right)'' = \frac{2}{\sigma^2}\left[\left(\frac{d\Theta_{MS}}{dR_{3D}}\right)^2 + \left(\frac{d\Phi_{MS}}{dR_{3D}}\right)^2\right] \tag{16}$$

The second derivative can be used to calculate the uncertainty of R_{3D}:

$$\sigma(R_{3D}) = \sqrt{\frac{2}{\left(\chi^2\right)''}} \tag{17}$$

With this method the three-dimensional track radius R_{3D} and its uncertainty σ can be obtained for each triplet which now need to be put together for the complete track. For a track consisting of n hits we have $n-2$ triplets and therefore $n-2$ radii. These are combined in the following way to obtain a radius $\overline{R_{3D}}$ for the track:

$$\overline{R_{3D}} = \sum_{i=1}^{n-2}\frac{R_{3D,i}}{\sigma_i(R_{3D})^2} / \sum_{i=1}^{n-2}\frac{1}{\sigma_i(R_{3D})^2} \tag{18}$$

with the uncertainty $\sigma(\overline{R_{3D}})$:

$$\sigma(\overline{R_{3D}}) = \left(\sum_{i=1}^{n-2} \frac{1}{\sigma_i(R_{3D})^2} \right) \tag{19}$$

Finally, the scattering angles are recalculated using the average radius completing the fitting procedure.

5 Vertex Fit

This section summarizes [17] and [18]. One characteristic of the signal event is that the three track originate from a common vertex. This can be used to suppress accidental background. To find this common vertex a vertex fit algorithm is implemented. For this, the track parameters have to be extrapolated through the inner detector layer to a common vertex region. Multiple scattering and the highly bent track in the magnetic field make this problem highly non-linear.

For the vertex fit spatial uncertainties are neglected and only multiple scattering in the inner detector layer is considered.

To describe the fit algorithm the same coordinate system as in the track fit is used: The z-axis is in direction of the magnetic field, x- and y-axis describe the plane transverse to it. θ, Θ describe polar angles, Φ, ϕ azimuthal angles.

The core idea behind the fit is to force the extrapolated tracks to bend in the 'right' direction to intersect with the vertex at $\vec{x}_V$ by introducing the scattering angles $\Phi_{MS,i}$ and $\Theta_{MS,i}$ for each track i. Then the χ^2 which has to be minimized is defined by equation (20). The uncertainties σ_Φ and σ_Θ are obtained from equation (4) and can be assumed to be equal in most cases.

$$\chi(\vec{x}_V)^2 = \sum_{i=1}^{3} \frac{\Phi_{MS,i}(\vec{x}_V)^2}{\sigma^2_{\Phi,i}} + \frac{\Theta_{MS,i}(\vec{x}_V)^2}{\sigma^2_{\Theta,i}} \tag{20}$$

As the functions $\Phi_{MS}(\vec{x_V})$ and $\Theta_{MS}(\vec{x_V})$ are in general non-linear, a linearisation approach around a estimated vertex position $\vec{x_{V,0}}$ is taken. There are different methods to find the first estimate for the vertex position. For example, its position in the transverse plane can be calculated using the two best measured tracks. The position in longitudinal direction can be calculated using the z-coordinate of the best measured track at this transverse position. The linearisation is then made by Taylor-expanding the scattering angles around the first estimate up to first order:

$$\begin{aligned}\Phi_{MS,i}(\vec{x}_V) &= \Phi_{MS,i}(\vec{x}_{V,0}) + \Delta\vec{x}_V \vec{\nabla}\Phi_{MS,i}(\vec{x}_{V,0}) \\ \Theta_{MS,i}(\vec{x}_V) &= \Theta_{MS,i}(\vec{x}_{V,0}) + \Delta\vec{x}_V \vec{\nabla}\Theta_{MS,i}(\vec{x}_{V,0})\end{aligned} \tag{21}$$

with $\vec{x}_V = \vec{x}_{V,0} + \Delta\vec{x}_V$.

The solution to the initial χ^2 problem is:

$$(\Delta\vec{x}_V)_k = -\frac{\sum_{i=1}^{3}\left[\frac{(\vec{\nabla}\Phi_{MS,i})_k \Phi_{MS,0,i}}{\sigma^2_{\Phi,i}} + \frac{(\vec{\nabla}\Theta_{MS,i})_k \Theta_{MS,0,i}}{\sigma^2_{\Theta,i}}\right]}{\sum_{i=1}^{3}\left[\frac{(\vec{\nabla}\Phi_{MS,i})^2_k}{\sigma^2_{\Phi,i}} + \frac{(\vec{\nabla}\Theta_{MS,i})^2_k}{\sigma^2_{\Theta,i}}\right]} \tag{22}$$

The algorithm can be iterated to improve the result by using $\vec{x}_{V,n+1} = \vec{x}_{V,n} + \Delta\vec{x}_V$ as next initial estimate.

6 Mass Reconstruction

After the simulation, the track fit is performed, delivering the track segments and their parameters for each frame. Then all possible segment combinations consisting of one segment with negative charge and two with positive charges are considered to try and find signal events. The charge of a segment is identified by its radius as electrons are assigned a positive and positrons a negative one. Then the vertex fit is applied using the parameters from the track fit. If no common vertex can be found because the tracks are badly reconstructed or simply do not share a common vertex this combination of tracks is rejected as the fit does not converge.

If a common vertex is found, the sum P_{sum} of the three 4-momenta P_i is calculated from the momenta $\vec{p_i}$ and the electron mass m_e assuming the three particles are electrons:

$$\begin{aligned}P_i &= (E_i, \vec{p_i}) \\ E^2 &= m^2 + p^2 \quad (c = 1) \\ P_i &= \left(\sqrt{p_i^2 + m_e^2}, \vec{p_i}\right) \\ P_{sum} = \sum_{i=1}^{3} P_i &= \sum_{i=1}^{3}\left(\sqrt{p_i^2 + m_e^2}, \vec{p_i}\right)\end{aligned} \tag{23}$$

Its magnitude $|P_{sum}|$ should be close to the muon mass if the combination was a signal event, see equation (2).

After this we still have combinations with reconstructed masses not near the muon mass because of internal conversion, accidental background not rejected yet, tracks with wrongfully assigned particle type, recurling tracks, etc. To separate the signal various cuts motivated by its properties can be performed. In the following some possible parameters to cut on are listed:

Total momentum

A fairly simple approach is to cut on the magnitude of the sum $\vec{p}_{tot}$ of the momenta $\vec{p}_i$ which should be close to zero for signal events, see equation (1).

Acoplanar momentum

Similar to the cut on total momentum, a cut on the acoplanar momentum p_{aco} which is the projection of the total momentum $\vec{p}_{tot}$ on the normal vector $\vec{t}$ of the decay plane can be performed:

$$\begin{aligned} \vec{v}_1 = \vec{p}_1 \times \vec{p}_2;\ \vec{v}_2 = \vec{p}_1 \times \vec{p}_3;\ \vec{v}_3 = \vec{p}_2 \times \vec{p}_3 \\ \vec{t} = \frac{\vec{v}_1}{v_1} + \frac{\vec{v}_2}{v_2} + \frac{\vec{v}_3}{v_3} \\ p_{aco} = \vec{p}_{tot} \cdot \vec{t} \end{aligned} \tag{24}$$

Vertex parameters

A cut on the position of the vertex can exclude tracks that do not originate from the target region or even from outside the detector.

A cut on the χ^2 of the vertex fit can exclude track combinations which do not share a common vertex to exclude accidental background.

Chapter III

Results

For this study I used the results of the simulation of the Mu3e experiment. The simulation parameters are those found in Appendix A if not stated otherwise. The base for the simulation is always the phase IA detector if not stated otherwise. As described in the introduction, the phase IA detector is the minimal design consisting only of target and two double detector layers.

It turns out that using a simple Gaussian to fit the occurring Gaussian-like distributions is often not quite satisfactory especially due to non-Gaussian tails. Therefore, another fairly simple approach is taken: The fit function is a sum of two normalized Gaussians with same mean μ but different σ (see eq. 25). The area weighted average sigma σ_{avg} is then referred as the resolution of the distributed value. This approach works better in most cases and delivers fits with χ^2/ndf closer to 1 than a simple Gauss fit.

$$\begin{aligned} A \cdot [(1-\epsilon) g_1(\mu, \sigma_1) + \epsilon g_2(\mu, \sigma_2)] \qquad \epsilon \in [0,1] \\ \sigma_{avg} = (1-\epsilon)\sigma_1 + \epsilon\sigma_2 \end{aligned} \tag{25}$$

7 Track Reconstruction

7.1 Momentum Resolution

One of the first properties to look at is the momentum resolution of the track reconstruction, as it defines the mass resolution and how good background, especially caused by internal conversion, can be suppressed. For the study of the momentum resolution, 100000 frames, each containing a signal event, were simulated and reconstructed to compare reconstructed and simulated momenta.

Settings

```
MuonRate =  0.1
SignalBF = 0.0
SpecialDecayMode = 1
100000 frames; one signal event per frame
```

In Figs. 15-17 the reconstructed momentum p_{rec} is plotted versus the 'true' momentum p_{MC} from the Monte Carlo simulation, which is contained in the reconstruction data, for track segments with 4, 6 or 8 hits. Most particle momenta range from about 14 MeV to 53 MeV which is about half the muon mass as expected. There are momenta higher than half the muon mass which are caused by muons decaying in flight and not at rest. A bias for reconstructed momenta lower than the true value is visible, especially for segments with more than four hits. Recurling particles hit the detector several times while losing energy, so the reconstructed momenta are smaller than the initially simulated ones. The resolution for segments with four hits decreases with higher momentum, because the high momentum tracks are less bent, which makes it difficult to calculate the radius and therefore the momentum accurately. This is not the case for segments with more hits, as these have to be highly bent to produce more than the initial four hits (see Fig. 18).

In Figs. 19-21 the difference between the reconstructed momentum p_{rec} and MC momentum p_{MC} is plotted for segments with four, six and eight hits and fitted with the function described above. For segments with four hits this results in a distribution with a RMS of 1.21 MeV and average sigma of 1.18 MeV. For higher hit number segments it is difficult to find an apt fit, as the distribution is asymmetric because of the bias for lower reconstructed momenta. Still, the resolution for tracks with more than four hits is improved to 0.22 MeV and 0.23 MeV, if the left tail of the distributions is ignored.

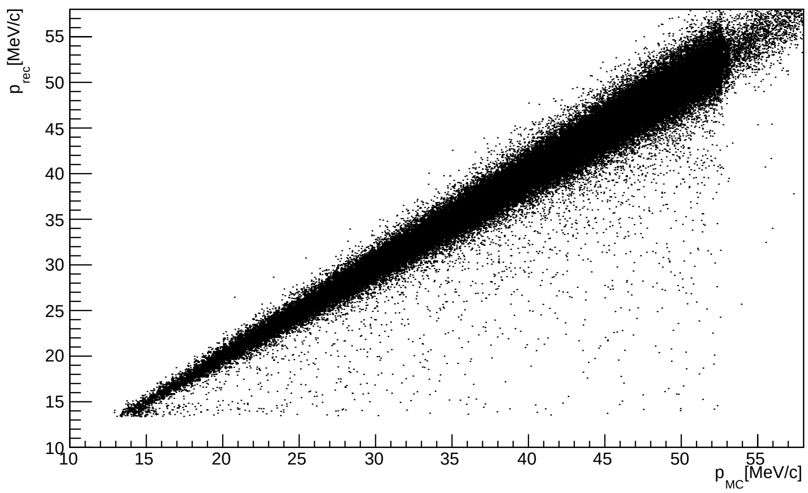

Figure 15: Reconstructed momentum vs MC momentum for segments with 4 hits.

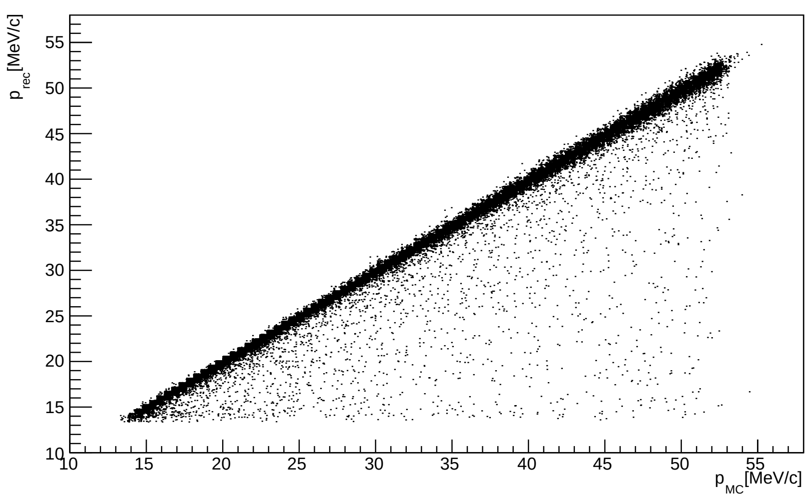

Figure 16: Reconstructed momentum vs MC momentum for segments with 6 hits.

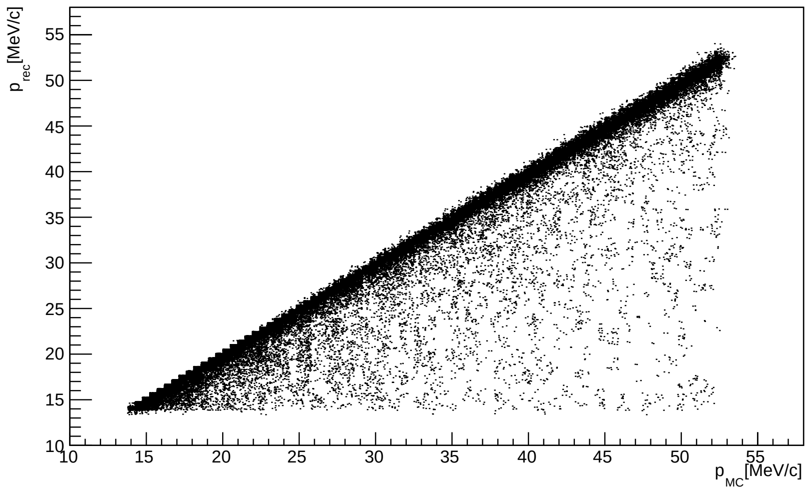

Figure 17: Reconstructed momentum vs MC momentum for segments with 8 hits.

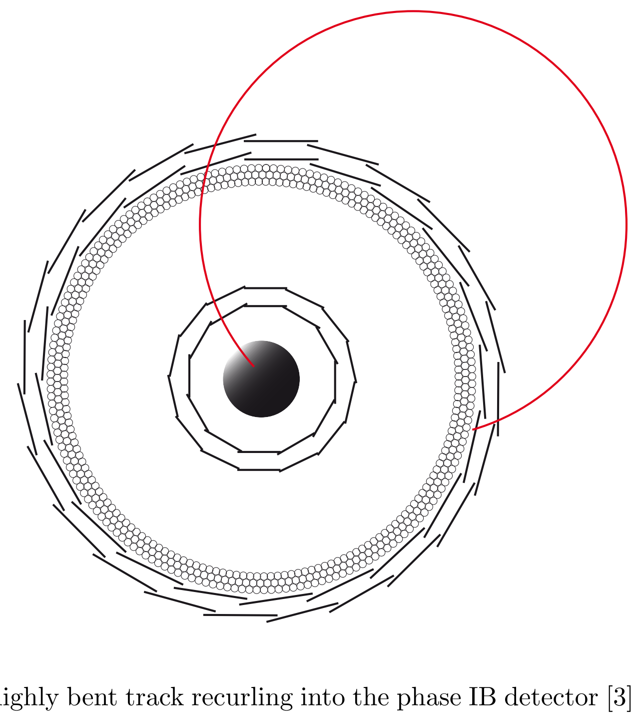

Figure 18: A highly bent track recurling into the phase IB detector [3]. In phase IA there are no fibre layers.

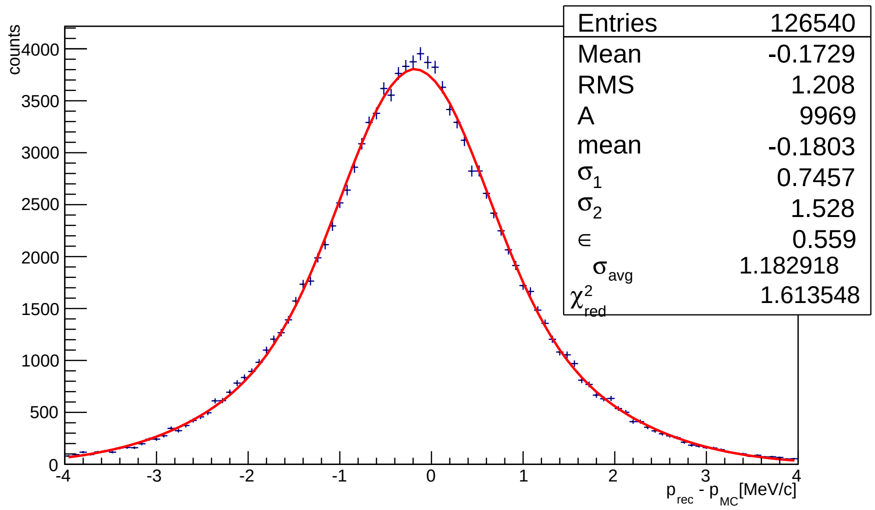

Figure 19: Momentum resolution for segments with 4 hits.

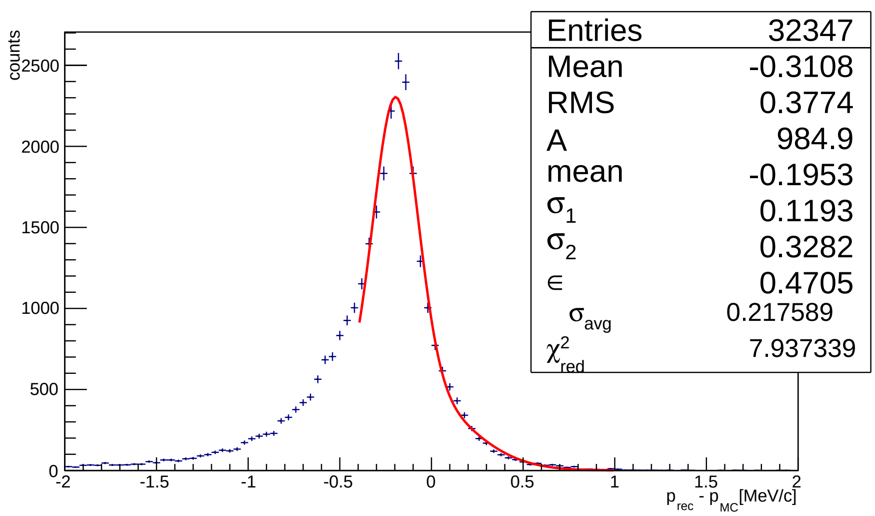

Figure 20: Momentum resolution for segments with 6 hits.

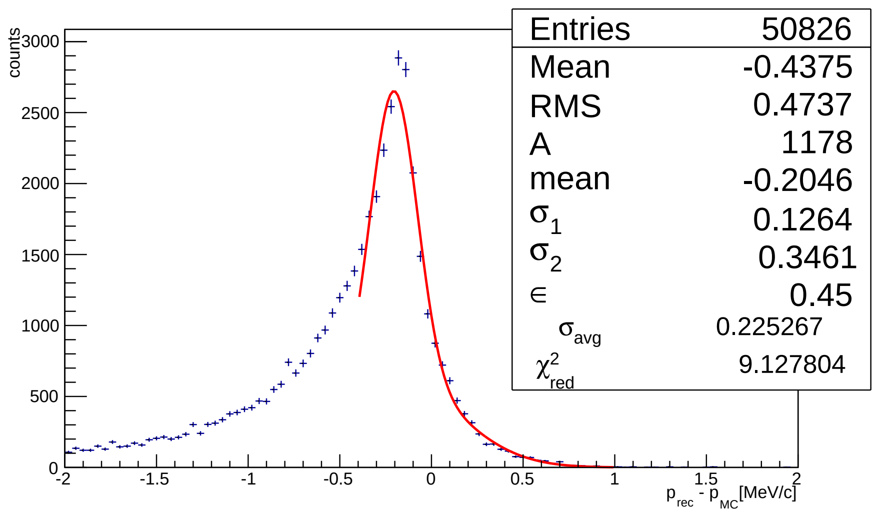

Figure 21: Momentum resolution for segments with 8 hits.

7.2 Track Finding Efficiency

Settings

```
MuonRate =  0.1
SignalBF = 0.0
SpecialDecayMode = 1
20000 frames; one signal event per frame
```

In this section the track finding efficiency —that is ratio of the number of tracks found by the reconstruction to the number of simulated tracks— is discussed. As the decay searched for is very rare the efficiency is required to be very high.
For this purpose one signal event per frame is simulated. Thus there are three tracks per frame. In Fig. 22 the efficiency of finding all simulated tracks in a momentum interval is plotted. The efficiency drops for lower momenta, going to zero at the minimum momentum of about 14 MeV, as the particles do not even reach the outer detector layer. Also, the efficiency with about 85% for high momenta is relatively low. This is because tracks that are not hitting the detector are considered. Particles can exit the detector without hitting a detecting layer if their inclination is too low and travel mostly in direction of the beamline.

The inclination in longitudinal direction is described by the 'dip' angle λ; $\lambda \in [-\frac{\pi}{2}, \frac{\pi}{2}]$. The dip angle is related to the azimuthal angle Θ introduced in the previous chapter: $\lambda = \frac{\pi}{2} - \Theta$. Large absolute values of λ correspond to trajectories close to the beamline, while λ close to zero corresponds to trajectories close to the transverse plane.

If only the efficiency of finding a track when the detector is actually hit is of interest, the counted simulated tracks can be restricted to a range of values for λ to make sure the tracks traverse the detector layers. In Fig. 23 the efficiency is shown with a restriction on λ: $|\lambda| \leq 0.8$.

In Fig. 24 the efficiency is plotted versus the dip angle λ. The decrease for high absolute values of λ is clearly visible. In this depiction again the efficiency is low, as low momentum tracks are also counted. Analogically to above, now the momentum can be constrained to $p \geq 15MeV$ to show the high efficiency for low absolute values of λ, as seen in Fig 25.

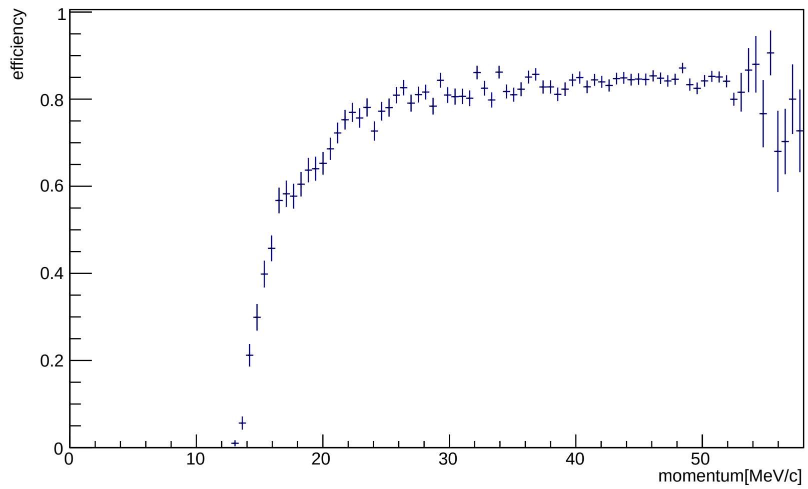

Figure 22: Efficiency of finding at least 4 hits of a track.

To summarize these depictions, Fig. 26 shows the efficiency dependence on momentum and angle, where the drop of the efficiency for low momenta and high absolute values of the dip angle can be seen. Also, there are some entries with muon mass larger than half the muon mass, as explained above. These mainly occur for $\lambda > 0$ corresponding to the direction of the beamline.

In Figs. 27 and 28 the same is plotted for segments with six and eight hits. The plots are significantly different to the one for four hits. Now, the track not only has to traverse the detector layers once in order to be detected, but also has to recurl to produce the additional hits. As seen, for higher momenta and higher absolute values of λ the track leaves the detector set-up without hitting enough detector layers. The higher the momentum, the smaller is the range of λ where the track can leave more than four hits and be detected as such. Because of this, the Mu3e detector will be augmented by adding recurl stations at both directions in phase IB and II.

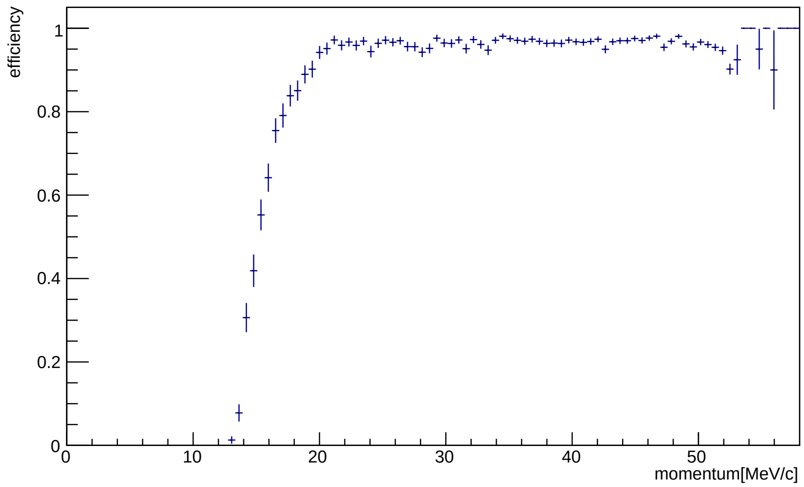

Figure 23: Efficiency of finding at least 4 hits of a track with restriction on dip angle ($|\lambda| < 0.8$).

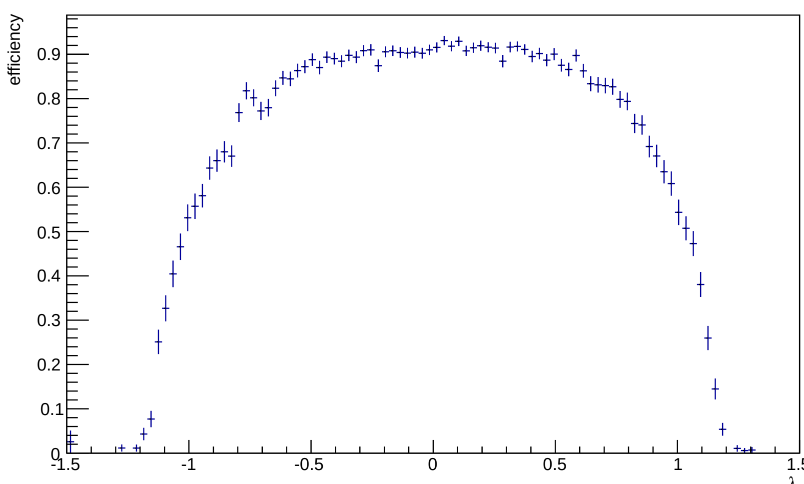

Figure 24: Track finding efficiency vs. dip angle for segments with at least 4 hits.

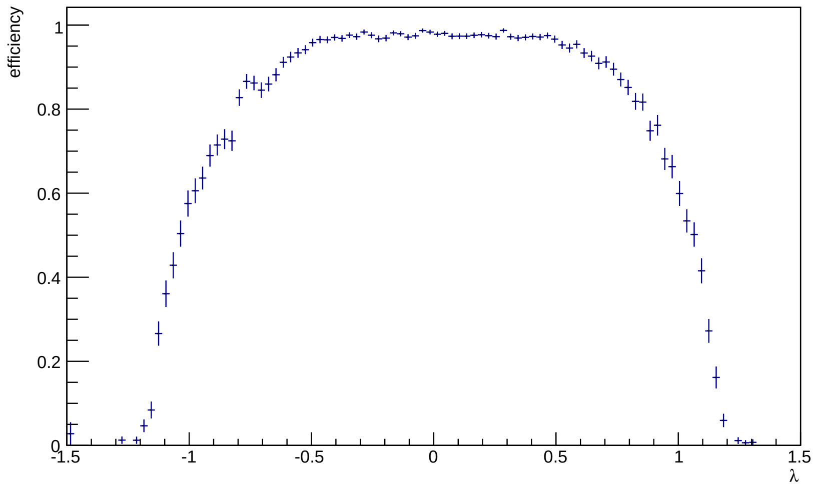

Figure 25: Track finding efficiency vs. dip angle for segments with at least 4 hits with restriction on momentum ($p > 15$ MeV).

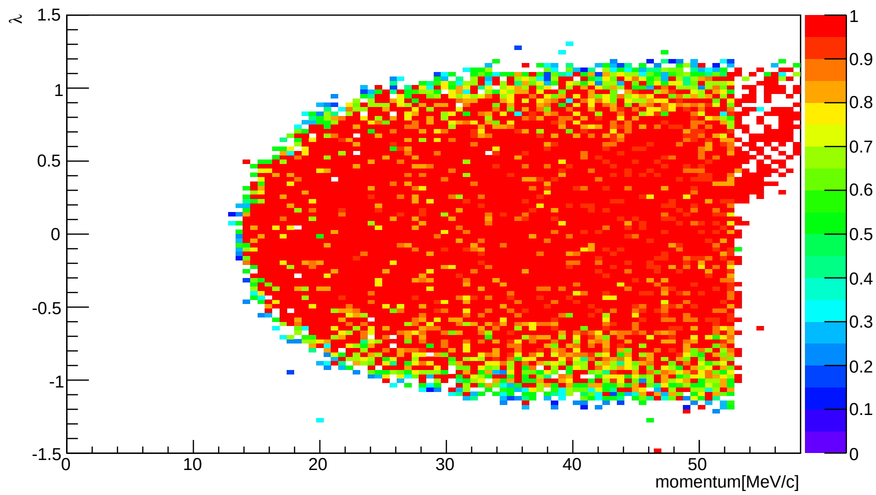

Figure 26: Track finding efficiency vs. momentum and dip angle for segments with at least 4 hits.

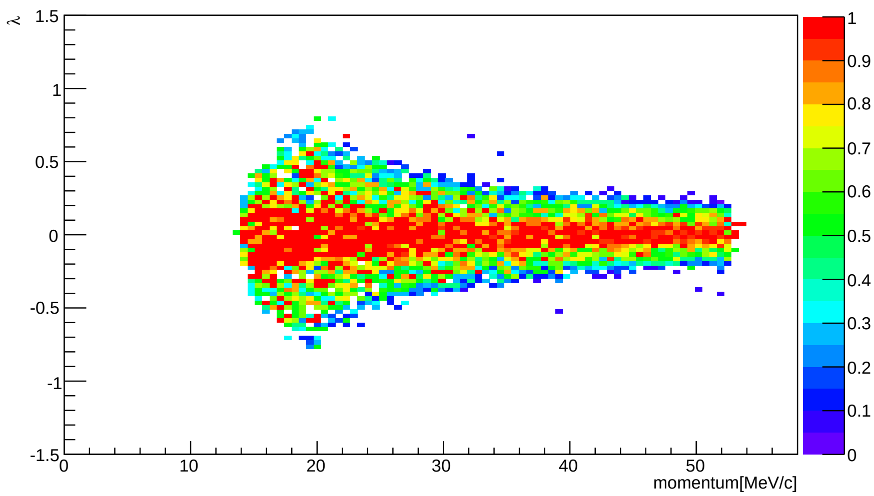

Figure 27: Track finding efficiency vs. momentum and dip angle for segments with at least 6 hits.

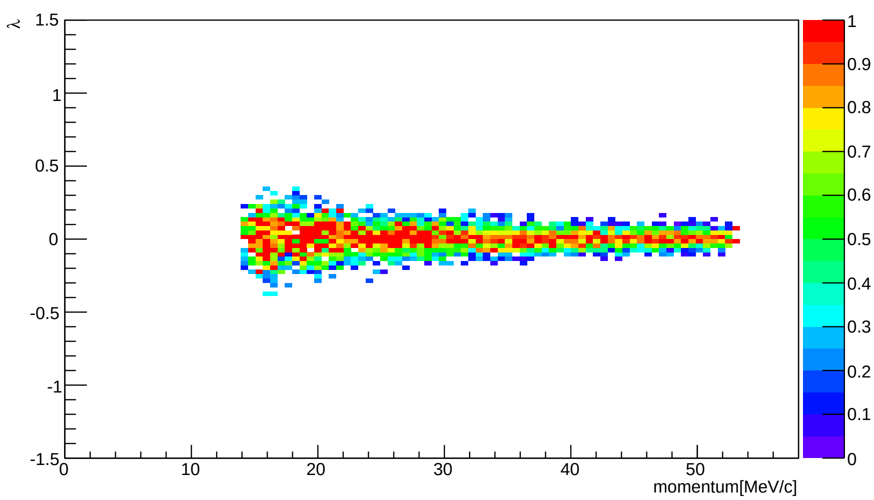

Figure 28: Track finding efficiency vs. momentum and dip angle for segments with at least 8 hits.

8 Vertex Fit

In [18] the properties of the vertex fit are studied with a simplified simulation. To make sure that the vertex fit works as intended in the more extensive simulation, some results of both studies are compared.

Settings

```
MuonRate                          =  0.1
SignalBF       = 0.0
SpecialDecayMode      = 1
20000 frames; one signal event per frame
```

8.1 Vertex Resolution

In Figs. 29-31 the vertex resolution in all three spatial coordinates after applying the cuts discussed below is shown for signal events. This delivers a resolution of $\sigma_{avg,x} = 0.219$ mm in the x-, $\sigma_{avg,y} = 0.234$ mm in y- and $\sigma_{avg,z} = 0.168$ mm in z-direction. In [18] the following values were found: $\sigma_x = 0.200$ mm, $\sigma_y = 0.195$ mm and $\sigma_z = 0.165$ mm. It should be noted that for this study a simple Gaussian was used to fit the distributions and multiple scattering inside the target was neglected.

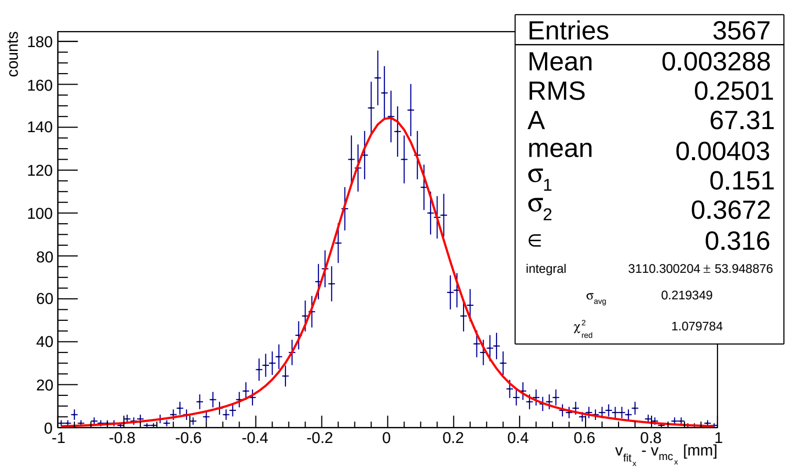

Figure 29: Vertex resolution x-position.

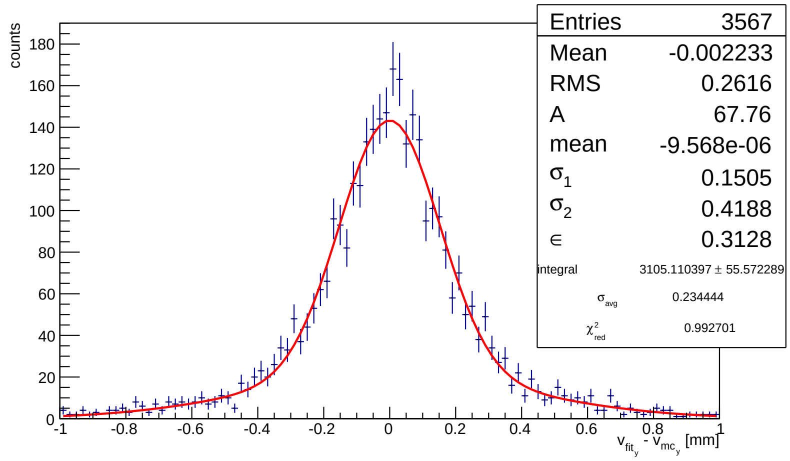

Figure 30: Vertex resolution y-position.

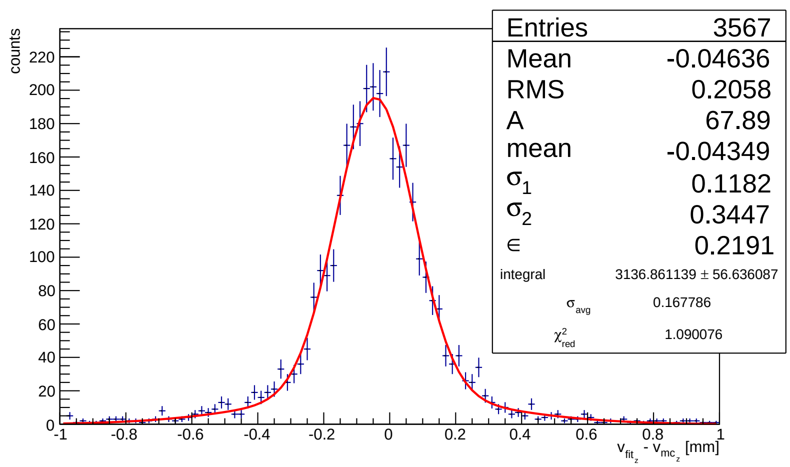

Figure 31: Vertex resolution z-position.

8.2 χ^2 Distribution

In Fig. 32 the χ^2 distribution for the vertex fit of signal events after applying cuts on total and acoplanar momentum discussed below is shown. The theoretical distribution is a χ^2 distribution with three degrees of freedom and therefore a mean value of three [18]. The mean value of the measured distribution is somewhat larger than that, indicating that the vertex fit does not fully take into account all sources of track errors, namely scattering in the target, pixel resolution and momentum resolution.

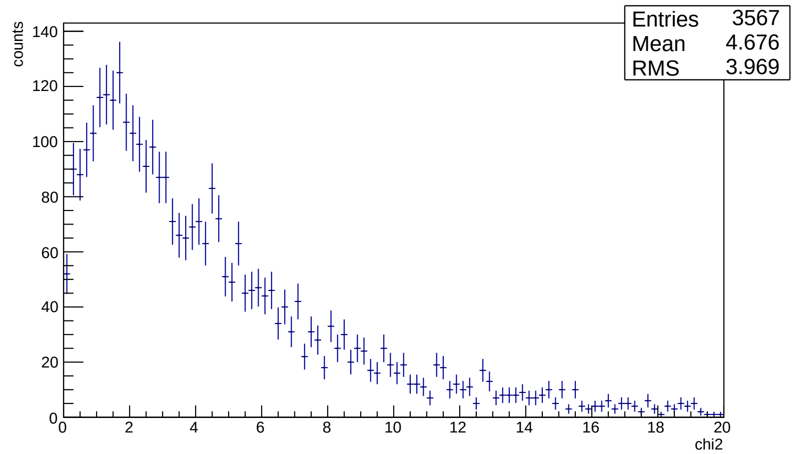

Figure 32: χ^2 distribution of vertex fit.

9 Mass Reconstruction

9.1 Cuts

Settings (Signal)

```
MuonRate =  0.1
SignalBF = 0.0
SpecialDecayMode = 1
20000 frames; one signal event per frame
```

Settings (Internal conversion)

```
 MuonRate                         =  0.1
 SignalBF      = 0.0
 SpecialDecayMode     = 21
21000 frames; one signal event per frame; done 200 times
```

To separate the signal from internal conversion background several cuts can be applied(see previous chapter). For this study cuts on the total and acoplanar momentum of the three decay particles and on the χ^2 of the vertex fit will be made. To determine the cuts, Figs. 33- 35 show each parameter over the reconstructed muon mass for signal events and Figs. 36- 38 for internal conversion. For this purpose 20000 frames with one signal event per frame and 200 times 21000 frames with radiative decay with internal conversion per frame were simulated.

The cuts $p_{tot} < 6.0$ MeV, $p_{aco} < 4.0$ MeV and $\chi^2 < 11$ seem reasonable.

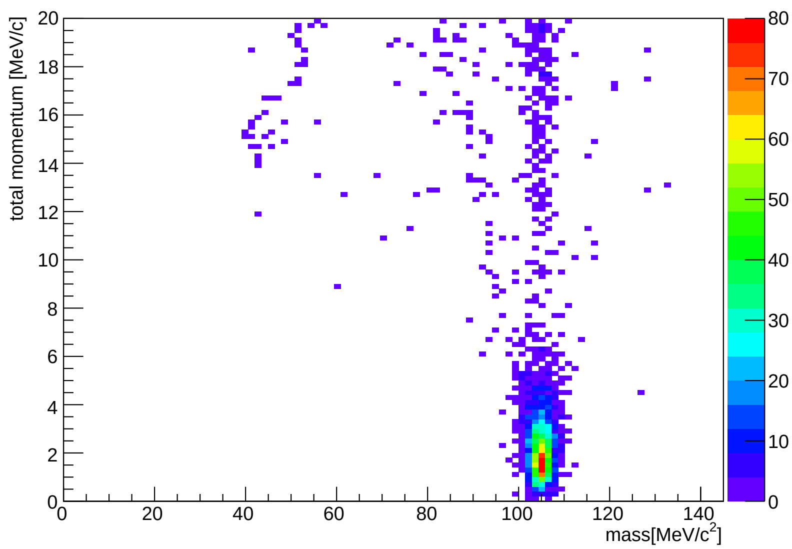

Figure 33: Reconstructed mass versus total momentum for signal events.

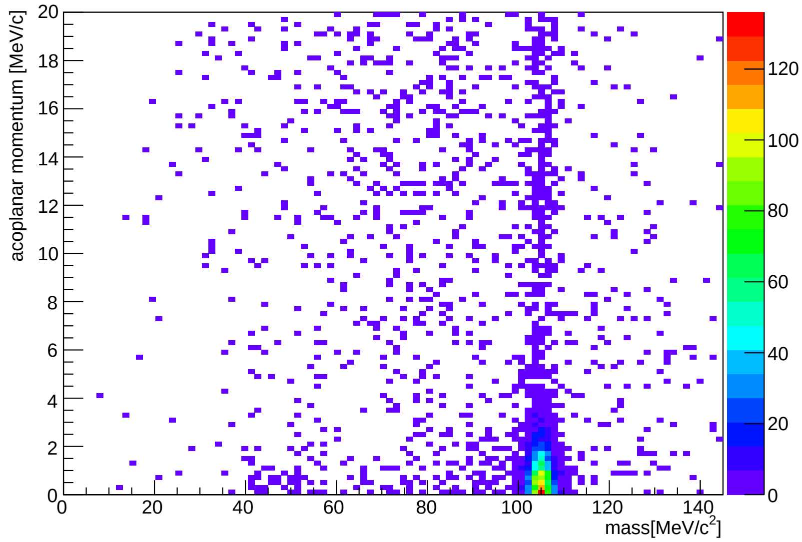

Figure 34: Reconstructed mass versus acoplanar momentum for signal events.

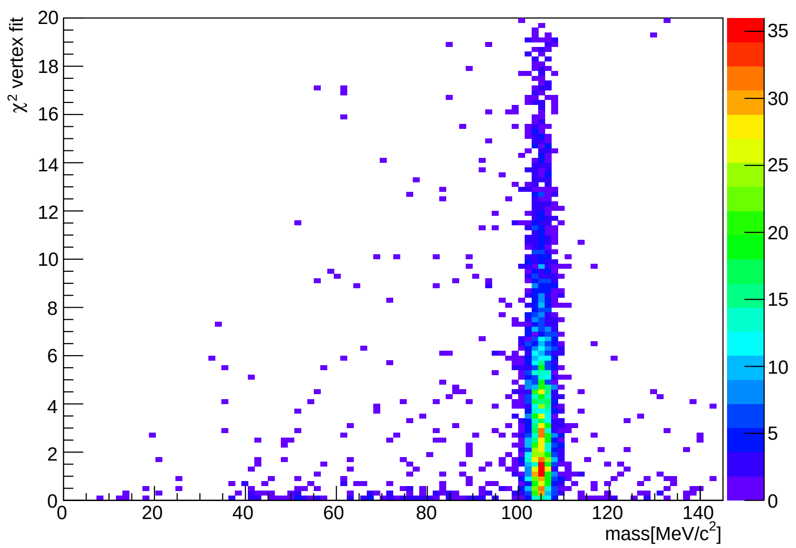

Figure 35: Reconstructed mass versus χ^2 of vertex fit for signal events.

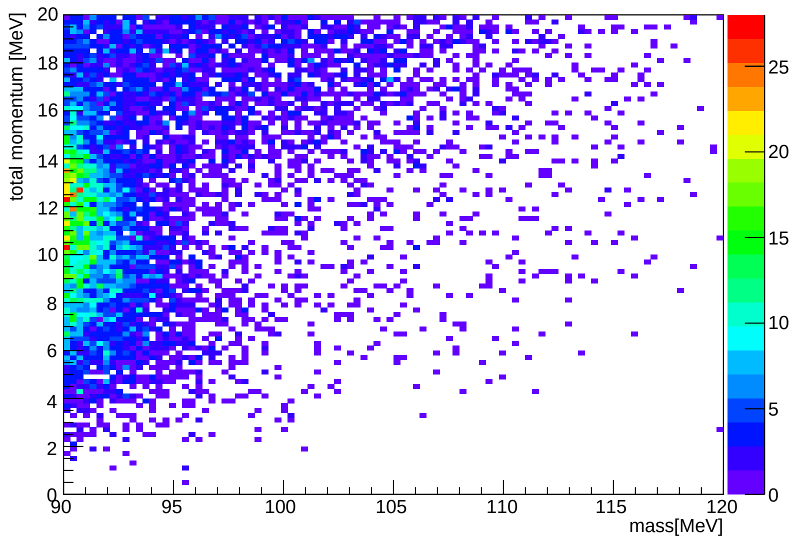

Figure 36: Reconstructed mass versus total momentum for internal conversion background.

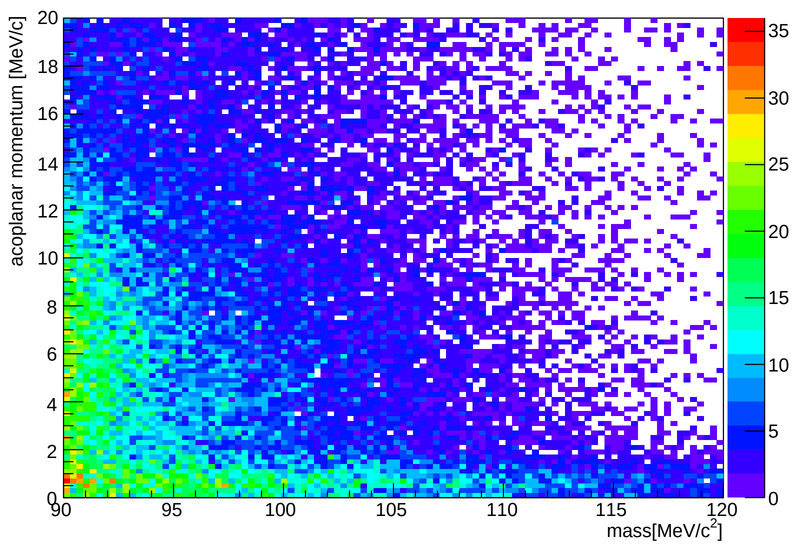

Figure 37: Reconstructed mass versus acoplanar momentum for internal conversion background.

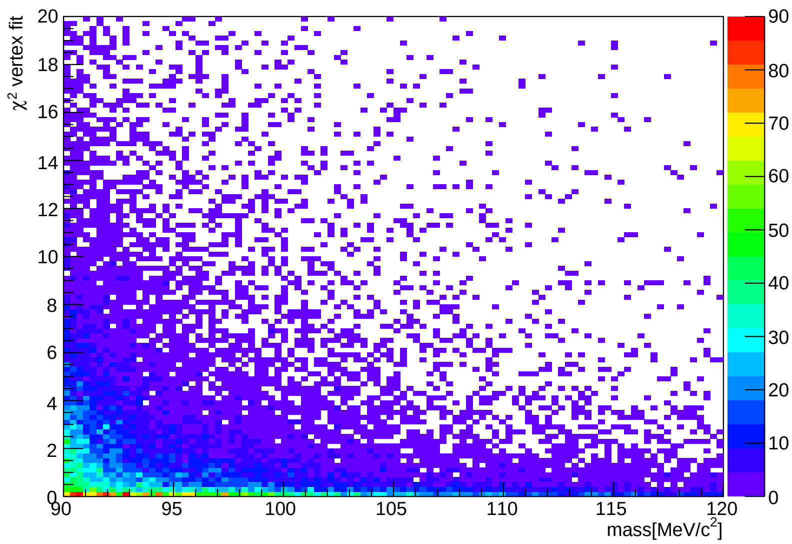

Figure 38: Reconstructed mass versus χ^2 of vertex fit for internal conversion background.

9.2 Mass Resolution

Settings

```
MuonRate =  0.1
SignalBF = 0.0
SpecialDecayMode = 1
DetectorPhase = 0; 1; 2
20000 frames; one signal event per frame
```

In the following the results of a simulation of 20000 signal events for all three detector phases are shown. Having only one signal per frame simplifies the mass reconstruction: Instead of having multiple combinations of segments filled in per frame, one can make sure that only one combination per frame is used. Which combination to use can be determined by looking at the total number of hits of all three tracks. As track segments with a higher number of hits should be measured more precisely, the first combination in a frame whose total number of hits is equal to the maximum number of hits of all combinations of a frame is chosen. Each track can have 4, 6 or 8 hits, so a combination of three tracks has 12 hits up to 24 hits. The cuts discussed in the previous section are applied. This means that the first combination in a frame which has the maximum number of hits and fulfils the cuts is filled in.

All three distributions are fitted with the function described at the beginning of this chapter. Apart from the fit parameters, the following values are given: 'σ_{avg}' is the mass resolution, as discussed above. 'Integral' is the number of entries in a $2\sigma_{avg}$ range around the mean value of the fit (denoted by 'mean'). With this the efficiency of finding and reconstructing a signal event can be calculated by dividing this number by the total number of simulated signal events. $\chi^2_{red} = \chi^2/ndf$ shows the χ^2 of the fit divided by the number of degrees of freedom.

In Fig. 39 the results of the mass reconstruction after the above described procedure are shown for phase IA. The peak around the muon mass is clearly visible. The distribution has a RMS of 1.795 MeV and the fit gives a mean value of 104.9 MeV with a resolution of $\sigma_{avg,IA} = 1.72$ MeV. The mass reconstruction efficiency is 14.6%.

Now the same is done for simulations of phase IB (Fig. 40) and phase II (Fig. 41). Even with the additional material introduced in the later phases increasing the effects of multiple scattering on the resolution, both show improved resolutions of $\sigma_{avg,IB} = 1.67$ MeV and $\sigma_{avg,II} = 1.64$ MeV. This is because the additional recurl stations allow more recurling tracks to be measured.

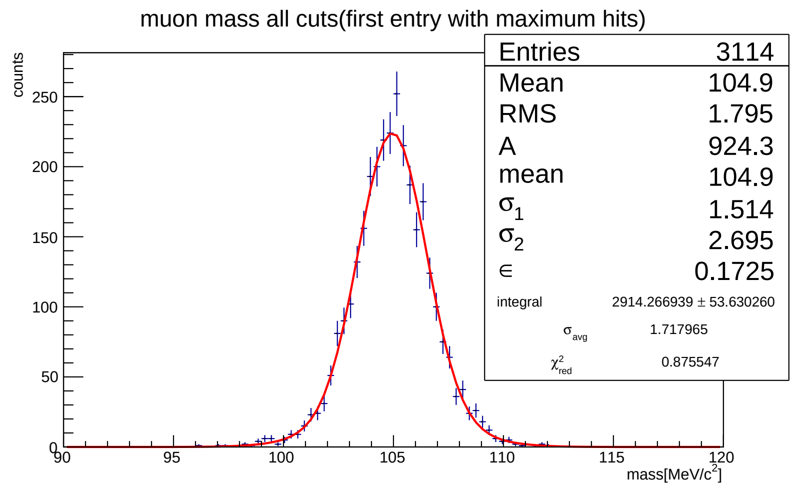

Figure 39: Mass resolution phase IA.

Settings

```
MuonRate =  0.1
SignalBF = 0.0
SpecialDecayMode = 1
DetectorPhase = 1
20000 frames; one signal event per frame
```

Settings

```
MuonRate =  0.1
SignalBF = 0.0
SpecialDecayMode = 1
DetectorPhase = 2
20000 frames; one signal event per frame
```

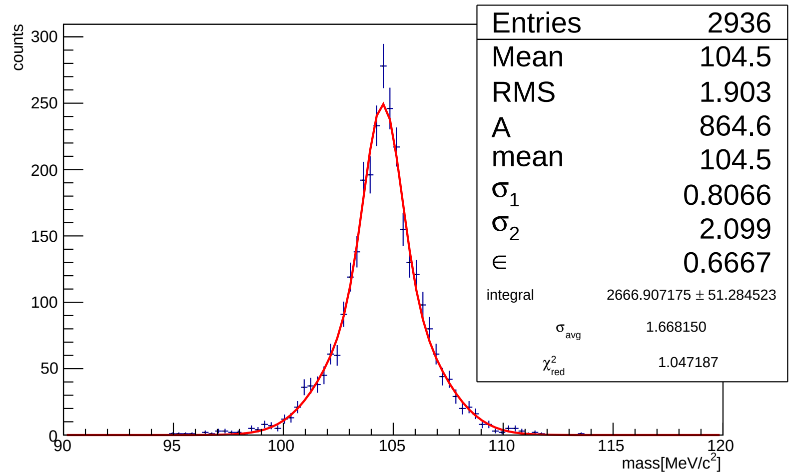

Figure 40: Mass resolution phase IB.

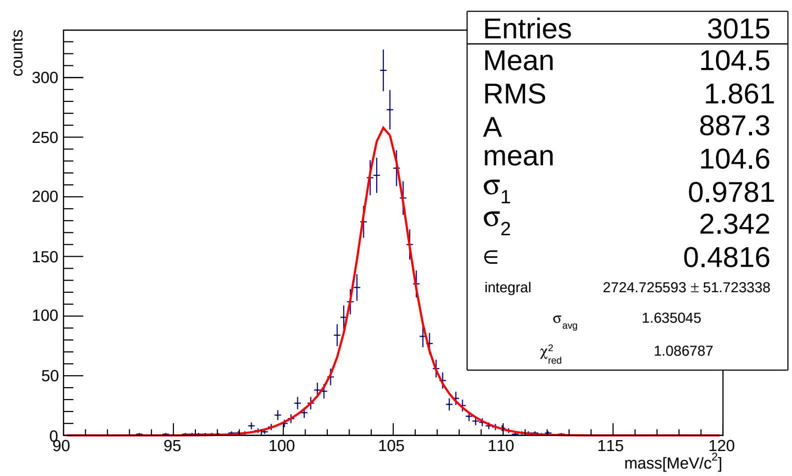

Figure 41: Mass resolution phase II.

9.3 Mass Resolution vs Tracker Thickness

Settings

```
MuonRate =  0.1
SignalBF = 0.0
SpecialDecayMode = 1
```

```
SmallSensorThickness = LargeSensorThickness varies

20000 frames for each detector thickness;
one signal event per frame
```

Fig. 42 shows the mass resolution for different sensor thicknesses of the inner and outer detector layers. For thicker detector layers the mass resolution gets worse, as the additional material increases multiple scattering. Note that for a thickness < 0.05 mm the tracker threshold had to be adjusted from 0.05 to 0.0005 to account for the lower efficiency for thinner detector layers. If the detector layer is too thin and the threshold too high, the particles can not deposit enough energy traversing the layer to be detected as hit. The lower threshold should not affect the resolution. For simplicity the fitting was done with a Gaussian distribution.

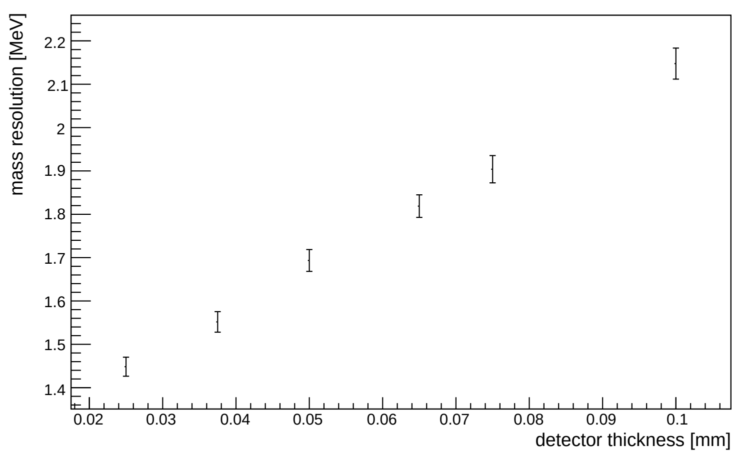

Figure 42: Mass resolution vs tracker thickness.

9.4 Multiple Scattering

Settings

```
MuonRate =  0.1
SignalBF = 0.0
SpecialDecayMode = 1
```

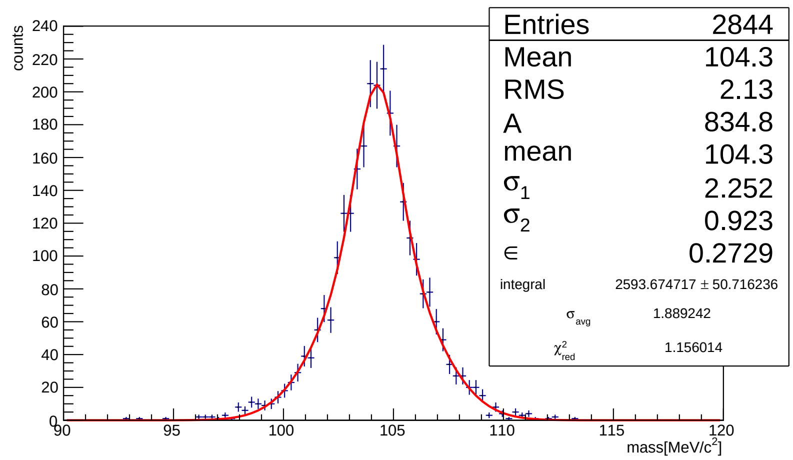

Figure 43: Signal for IB with increased number of fibre layers.

```
NFibreLayers = 5
DetectorPhase = 1

20000 frames; one signal event per frame
```

An easy way to show the effect of multiple scattering on the mass resolution is to increase the material in the detector by increasing the number of fibre layers. In Fig. 43 shows the result of the simulation of phase IB with increased number of fibres layer from 3 to 5. The mass resolution is now $\sigma_{avg} = 1.89$ MeV. This a significant difference to the resolution determined for the same set-up with 3 fibres of 1.67 MeV.

9.5 Signal Efficiency vs. Tracker Efficiency

Settings

```
MuonRate = 0.1
SignalBF = 0.0
SpecialDecayMode = 1
TrackerEfficiency  values from 0.8 to 1.0

20000 frames for each tracker efficiency;
```

```
one signal event per frame
```

In Fig. 44 the efficiency of reconstructing signal events is shown against the tracker efficiency. For simplicity, the mass distributions were fitted with Gaussians and the events in the 2σ region were counted. Because at least four hits are needed to reconstruct a track and in total 12 hits to reconstruct the mass, the efficiency should go down as 12th power of the tracker efficiency. Therefore, the simple function Ax^{12} was fitted to the resulting graph to show the expected relation.

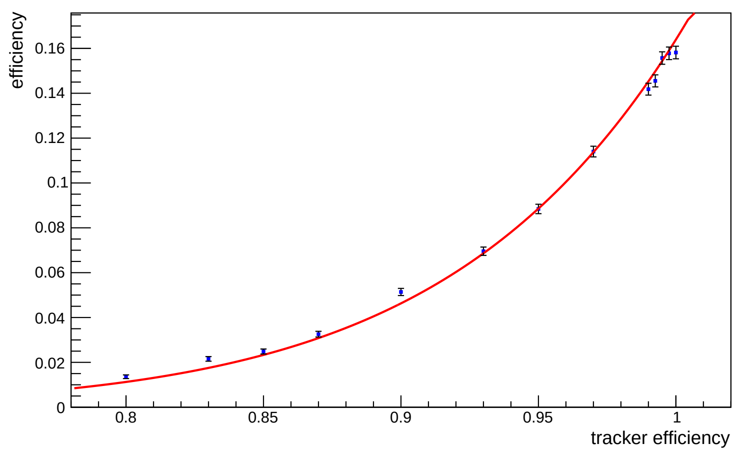

Figure 44: Signal efficiency vs tracker efficiency.

9.6 Mass Resolution vs. Pixel Size

Settings

```
MuonRate =  0.1
SignalBF = 0.0
SpecialDecayMode = 1
SmallSensorPixelSize = LargeSensorPixelSize = 0.07; 0.09; 0.16

20000 frames for each pixel size;
one signal event per frame
```

In Figs. 45-47 the mass resolution is shown for different pixel sizes of the detector. As expected, the resolution gets better with smaller pixel sizes and worse with larger pixel sizes, as the spatial resolution changes with the pixel size. Also, a change in the efficiencies for different pixel sizes can be observed. This due the small gaps between the overlapping detector tiles. In this area the pixel size becomes important for the reconstruction and the pixel size influences the efficiency, if not taken into account properly.

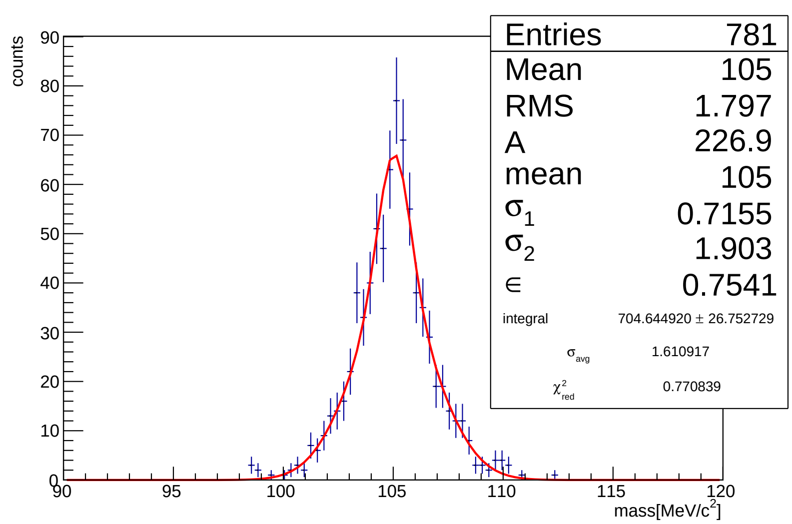

Figure 45: Reconstructed mass with pixel size of 0.07mm.

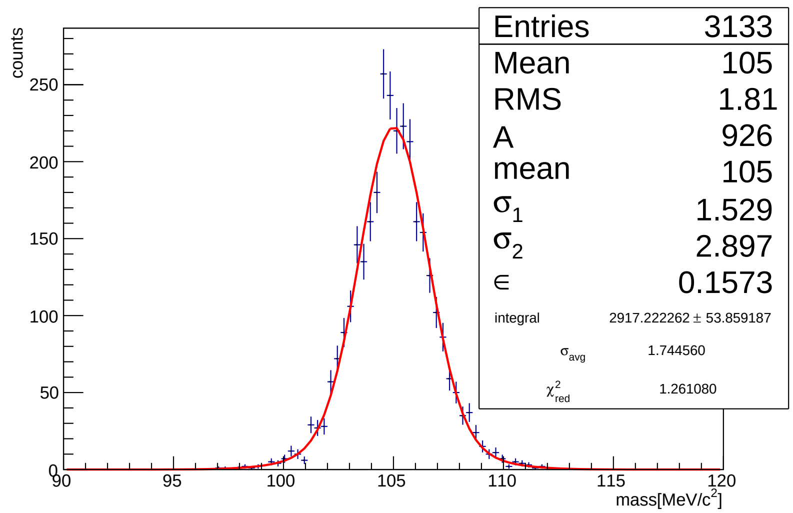

Figure 46: Reconstructed mass with pixel size of 0.09mm.

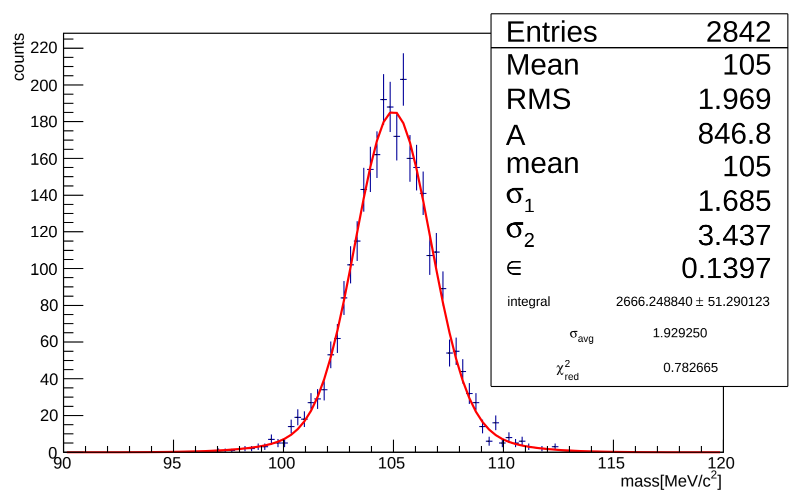

Figure 47: Reconstructed mass with pixel size of 0.16mm.

9.7 Internal Conversion

Settings

```
MuonRate =  0.1
SignalBF = 0.0
SpecialDecayMode = 21
InternalConversionMassCut = 80

21000 frames; one signal event per frame;
repeated 200 times
```

For the study of the internal conversion background $4.2 \cdot 10^6$ frames in total were simulated with one radiative decay with internal conversion each. In Fig. 48 and Fig. 49 the reconstructed masses are shown without applying any cuts. As described in the previous chapter only internal conversion events fulfilling certain restrictions, for example on the invariant mass, are simulated in the end.

In Fig. 50 the reconstructed masses are shown after applying the same cuts as for the signal in the above section. From this a sensitivity limit can be calculated. First, from the branching fraction of internal conversion decays the total number of decayed muon can be determined: From [4] the branching fraction $r_{IC} = 3.4 \cdot 10^{-5}$ can be obtained. The simulation software delivers the fraction of internal conversion decays fulfilling the restrictions. For the settings used here, this fraction is $r_{sim} = 5.231 \cdot 10^{-5}$. The total branching fraction is then $r_{tot} = r_{IC} \cdot r_{sim} = 1.78 \cdot 10^{-9}$. The total number of muons, which would need to decay for $4.2 \cdot 10^6$ internal conversions to be generated at this ratio, is then $N = \frac{4.2 \cdot 10^6}{1.78 \cdot 10^{-9}} \approx 2.4 \cdot 10^{15}$ muons.

There are no background events left in the $2\sigma_{avg}$ range around the fitted muon mass. For this case the upper limit UL for the sensitivity can be calculated with equation (26) at a 95 % confidence level [19].

$$UL = \frac{-\log(1-0.95)}{N\varepsilon} \approx \frac{2.996}{N\varepsilon} \tag{26}$$

with $N \approx 2.4 \cdot 10^{15}$ the total number of muons and $\varepsilon \approx 0.146$ the signal finding efficiency. With this, the expected upper limit in case no signal is observed is $UL = 8.6 \cdot 10^{-15}$.

For phase IA it is planned to have a muon stopping rate on the target of $2 \cdot 10^7 Hz$ [3]. With this rate it would take about 3.8 years of data taking to get $2.4 \cdot 10^{15}$ decayed muons to reach this sensitivity. The πE5 beamline at PSI is the most intense muon beamline currently available, delivering up to $1 \cdot 10^8 \frac{muons}{s}$. This rate would reduce the data taking time to about 280 days.

To reach the desired sensitivity of 10^{-6}, a new high intensity beamline is needed, providing rate of larger than $1 \cdot 10^9 \frac{muons}{s}$.

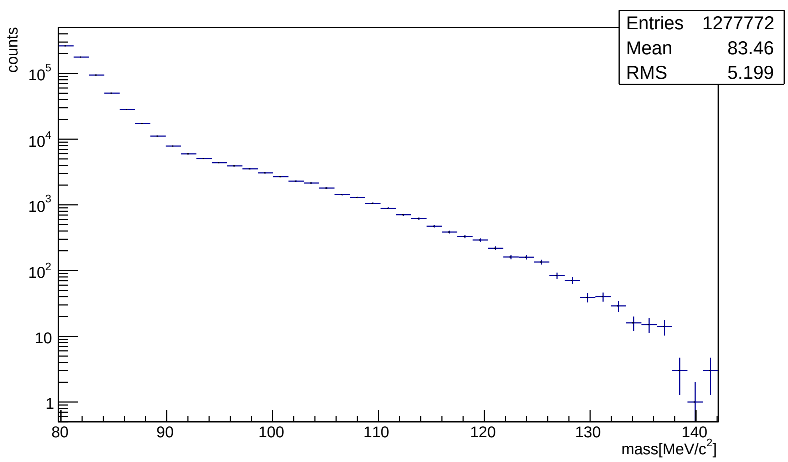

Figure 48: Reconstructed mass for internal conversion background.

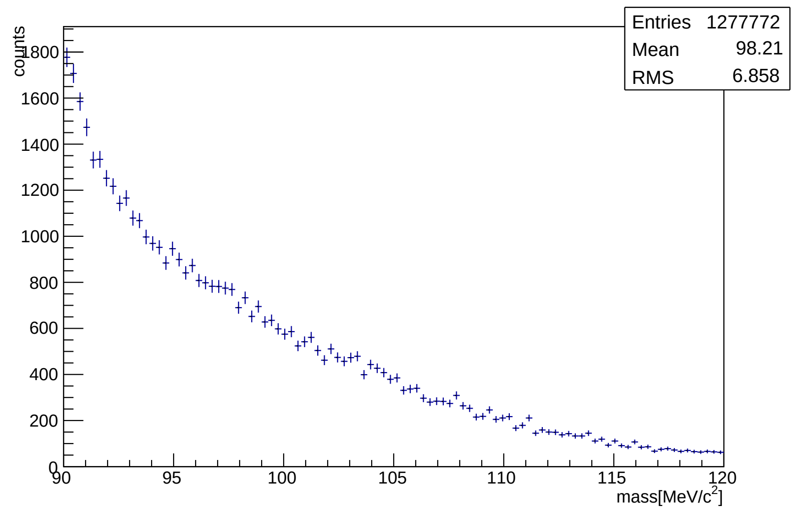

Figure 49: Reconstructed mass for internal conversion background in signal region.

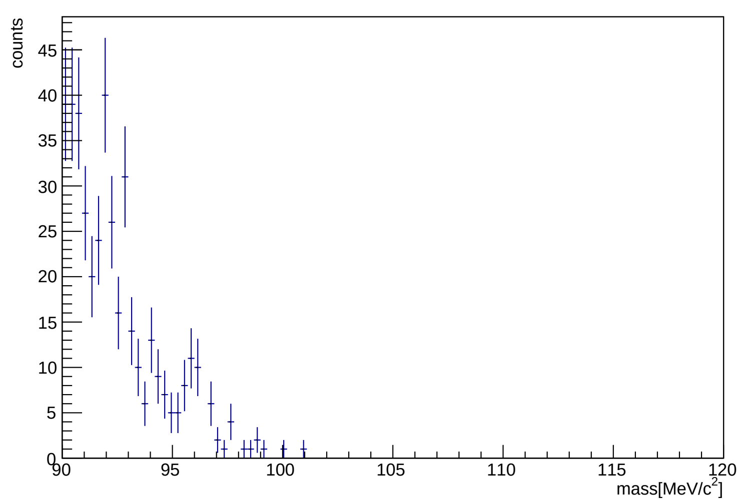

Figure 50: Reconstructed mass for internal conversion background in signal region after cuts.

Chapter IV

Conclusion

10 Summary

In this study, various properties of the software, which will be used in the Mu3e experiment, have been tested. So far, the results seem to agree with the expected behaviour.

First, the momentum resolution of the phase IA detector for tracks consisting of different number of hits was examined. A resolution of 1.18 MeV for 4-hit tracks and a resolution of about 0.22 MeV for 6- and 8-hit tracks was measured.

The vertex fit delivers resolutions of about 0.17 to 0.23 mm depending on the spatial direction. These results are similar to those found in previous studies.

The efficiency of finding at least four hits of a track are very high for the most part, whereas the efficiencies of finding at least six or eight hits are only high in small regions.

The simulation was done with different pixel sizes of the detector to show the influence of the spatial resolution of the hit positions on the mass resolution.

The signal efficiency was examined for different tracker efficiencies.

The influences of multiple scattering on the mass resolution were shown by introducing more material in the detector.

For the phase IA detector cuts on total and acoplanar momentum and χ^2 were made, resulting in a mass resolution of 1.72 MeV and eliminating all background in a two σ region around the determined mean of the signal peak. This allowed to estimate an expected upper limit of $8.6 \cdot 10^{-15}$.

11 Outlook

As the software used in this study is still under ongoing development, similar studies in the future could yield different results than those presented here. There are still some points where the software will be improved.

The efficiency of finding tracks with more than four hits should increase in later detector phases by adding recurl stations. Therefore, the mass resolution should improve, even with the additional material in the detector, allowing to push down the sensitivity limit even further.

The vertex fit still can be improved to increase the vertex resolution by taking neglected sources of uncertainties into account.

The track reconstruction can be improved to not require all hits to find a track, increasing the signal efficiency.

This study did not consider accidental and combinatorial background, so further research should be done in that direction. Also, it would be of interest to simulate a 'real' run of the experiment, where not only one event is simulated per frame, which is especially important for higher muon rates and later detector phases.

Appendix A

Simulation Configurations

```
************************************************
***          Digi Configuration             ***
************************************************

ReadoutFrameLength          = 50
MuonRate                    =  0.1
SignalBF      = 0.0
SpecialDecayMode     = 0
* 0 for none,
* 1 for one signal decay per frame
* 2-19 overlays of two or three decays from the same vertex
* With S signal, M michel, R radiative and I internal conversion
* 2:  SS
* 3:  MM
* 4:  MR
* 5:  MI
* 6:  RR
* 7:  RI
* 8:  II
* 9:  SSS
* 10: MMM
* 11: MMR
* 12: MRR
* 13: RRR
* 14: MMI
* 15: MII
```

```
* 16: III
* 17: MIR
* 18: RRI
* 19: RII
* 20: One (guaranteed) radiative decay per frame
* 21: One (guaranteed) radiative decay with internal conversion per frame

InternalConversionSelectionType   = 0
* 0: Cut on all three electrons
* 1: Cut on at least one e+e- pair
InternalConversionCosThetaCut     = 0.8
InternalConversionEminCut         = 10
InternalConversionEvisCut         = 0
InternalConversionMassCut  = 80

MuonPolarization     = 1.0

BeamSizeX      = 5
BeamSizeY      = 5
BeamDivergenceX      = 0.05
BeamDivergenceY      = 0.05
BeamMomentumSpread      = 1
BeamMomentumCorrection       = 3

WriteTruth = 1
WriteTarget = 1
WritePixels = 1
WriteFibres     = 1
WriteTiles = 1

# Set to zero for switching off readout simulation
TrackerMaxHitsFrameInner  = 5
TrackerMaxHitsFrameOuter  = 2

TrackerEfficiency          = 1.0
InnerTrackerNoiseRate  = 0
OuterTrackerNoiseRate  = 0

TrackerThreshold  = 0.005
```

```
FibreTimeResolution          = 0.4
FibreZResolution             = 15
FibreEnergyPerPhoton         = 0.0001
FibreEfficiency              = 0.005
FibreDeadtime      = 1
FibreSipmQE      = 0.5
* amplitude per photon in mV
FibreAmplitudePerPhoton      = 20
FibrePhotonThreshold         = 1
*Time resolution in ns for 1.217 MeV energy depostition
TileTimeResolution           = 0.09

*Energy resolution in %
TileEnergyResolution         = 0.1

*Deadtime for 1.217 MeV energy deposition
TileDeadtime      = 150

TrajectoryMomentumCutoff     = 3
TargetHitMomentumCutoff  = 10

ScatteringModel              = 1
* 0: Single, 1: Urban, 2: Goudsmit, 3:Wentzel

*************************************************

#************************************************
#***           Detector Configuration          ***
#************************************************
#
# Units are mm and Tesla

WorldLength  = 3200
WorldWidth  = 1500
WorldHeight  = 1500

# 0 for phase 1a
# 1 for phase 1b
```

```
# 2 for phase 2
DetectorPhase        = 0

TargetThickness1      =    0.03
TargetThickness2      =    0.08
TargetLength         =   50.0
TargetRadius         =   10.0

SmallSensorLength    =   20.0
SmallSensorWidth     =  10.0
SmallSensorThickness =    0.05
SmallSensorOverhang  =   1.0
SmallSensorDeadWidth =    0.5
SmallSensorPixelSize =    0.08
SmallSensorOffset    =   0.5

LargeSensorLength    =   20.0
LargeSensorWidth     =  20.0
LargeSensorThickness =   0.05
LargeSensorOverhang  =   1.0
LargeSensorDeadWidth =    0.5
LargeSensorPixelSize =   0.08
LargeSensorOffset    =   0.5

KaptonThickness      =   0.05
KaptonOverlength     =  20.0

ConductorThickness   =    0.015
ConductorWidth       =    5.0

NSmallLayers         =    2
NLargeLayers         =    2

NPhiSensorsLayer1    =   12
NPhiSensorsLayer2    =   18
NPhiSensorsLayer3    =   24
NPhiSensorsLayer4    =   28

NZSensorsSmall   = 6
```

```
NZSensorsLarge       = 18


FibreDiameter   =    0.25
FibreRadius     =   60.0
FibreLength     =  360.0
NFibreLayers =   3

NPhiRecurlScintillatorTiles = 48
NZRecurlScintillatorTiles = 48

RecurlScintillatorRadiusOuter = 65.3280739055101805
RecurlScintillatorRadiusInner = 60.3280739055101805

MagnetInnerRadius    =  500.0
MagnetOuterRadius    =  550.0
MagnetLength         = 3000.0
# 0 for no field
# 1 for constant Bz field
# 2 for COBRA field
# 3 for solenoid field with spin tracking
# 4 for solenoid
# 5 for realistic thin solenoid, including radial components
# 6 for field from a field map
MagneticFieldConfiguration = 6
MagneticFieldStrength = 1.0
Fieldmap = field.bin
TransportFieldStrength = 1.5

BeampipeOuterRadius = 25.0
BeampipeInnerRadius = 15.0
BeampipeEndpoint = 80.0

ZCollimator1        = -200.0
ZCollimator2        = -1300.0
#**************************************************
```

Bibliography

[1] Wikimedia commons, standard model of elementary particles, [Online; accessed 19.08.2014].

[2] U. Bellgardt et al., [SINDRUM Collaboration], *"Search for the Decay $\mu^+ \rightarrow e^+e^+e^-$"*, Nucl.Phys., **B299** 1, 1988.

[3] A. Blondel et al., *"Research Proposal for an Experiment to Search for the Decay $\mu \rightarrow eee$"*, ArXiv e-prints, January 2013, (`arXiv:1301.6113 [physics.ins-det]`).

[4] J. Beringer et al. (Particle Data Group), *"Review of Particle Physics (RPP)"*, Phys.Rev., **D86** 010001, 2012.

[5] R. M. Djilkibaev and R. V. Konoplich, *"Rare Muon Decay $\mu^+ \rightarrow e^+e^-e^+\nu_e\bar{\nu_\mu}$"*, Phys.Rev., **D79** 073004, 2009, (`arXiv:0812.1355 [hep-ph]`).

[6] F. Förster, *"HV-MAPS Readout and Direct Memory Access for the Mu3e Experiment"*, Master's thesis, Heidelberg University, 2014.

[7] A. Damyanova, *"Development of a Scintillating Fibre Tracker/Time-of-Flight Detector with SiPM Readout for the Mu3e Experiment at PSI"*.

[8] C. Licciulli, *"Präzise Zeitmessung für das Mu3e-Experiment"*, Master's thesis, Heidelberg University, 2013.

[9] P. Eckert, *The Mu3e Tile Detector*, PhD thesis, Heidelberg University, in preparation.

[10] S. Agostinelli et al., *"Geant4–a simulation toolkit"*, Nucl. Instr. Meth., **A 506**(3) 250 – 303, 2003.

[11] W.E. Fischer and F. Scheck, *"Electron Polarization in Polarized Muon Decay: Radiative Corrections"*, Nucl.Phys., **B83** 25, 1974.

[12] F. Scheck, *"Muon Physics"*, Phys.Rept., **44** 187, 1978.

[13] P. Depommier and A. Vacheret, Radiative muon decay, Technical report, TWIST Technote No 55, 2001.

[14] C. Fronsdal and H. Überall, *"μ-Meson Decay with Inner Bremsstrahlung"*, Phys. Rev., **113** 654–657, Jan 1959.

[15] R. Kleiss, W.J. Stirling and S.D. Ellis, *"A new Monte Carlo treatment of multiparticle phase space at high energies"*, Comp. Phys. Commun., **40** 359 – 373, 1986.

[16] A. Schöning, A three-dimensional helix fit with multiple scattering using hit triplets.

[17] A. Schöning, Linearised vertex 3d fit in a solenoidal magnetic field with multiple scattering.

[18] S. Schenk, *"A Vertex Fit for Low Momentum Particles in a Solenoidal Magnetic Field with Multiple Scattering"*, Bachelor's thesis, Heidelberg University, 2013.

[19] S. Corrodi, *"Fast Optical Readout of the Mu3e Pixel Detector"*, Master's thesis, ETH Zurich and Heidelberg University, 2014.

Acknowledgements

An dieser Stelle möchte ich allen danken, die diese Arbeit ermöglicht haben.

An erster Stelle möchte ich mich bei Herrn Dr. Niklaus Berger, der mich auf das Mu3e-Experiment aufmerksam gemacht hat und immer für Fragen offen stand, für die Betreuung beim Schreibprozess und die Korrektur dieser Arbeit bedanken.

Als Nächstes möchte ich mich bei meinen Bürokollegen Dr. Alexandr Kozlinskiy, Dr. Shruti Shrestha, Sebastian Schenk und Moritz Kiehn für die freundliche Arbeitsatmosphäre und all die Hilfe bei Problemen bedanken. Bei Moritz Kiehn möchte ich mich nochmals für das Korrekturlesen und die Vorschläge zu dieser Arbeit bedanken.

Ebenfalls danke ich dem Rest der Gruppe für die angenehme Arbeitsatmosphäre.

Bei Prof. Dr. Stephanie Hansmann-Menzemer, die sich sofort bereit erklärt hat, die Zweitkorrektur zu übernehmen, möchte ich mich ebenfalls bedanken.

Abschließend möchte ich mich bei meiner Familie und bei meinen Freunden für die Unterstützung während meines gesamtem Studiums bedanken.

Erklärung

Ich versichere, dass ich diese Arbeit selbstständig verfasst und keine anderen als die angegebenen Quellen und Hilfsmittel benutzt habe.

Heidelberg, den ...., ...